

The flavor composition of ultra-high-energy cosmic neutrinos: measurement forecasts for in-ice radio-based EeV neutrino telescopes

Alan Coleman,^{*} Oscar Ericsson, and Christian Glaser[†]

Department of Physics and Astronomy, Uppsala University, Uppsala, SE-752 37, Sweden

Mauricio Bustamante[‡]

*Niels Bohr International Academy, Niels Bohr Institute,
University of Copenhagen, DK-2100 Copenhagen, Denmark*

(Dated: February 6, 2024)

In-ice radio-detection is a promising technique to discover and characterize ultra-high-energy (UHE) neutrinos, with energies above 10^{17} eV, adopted by present—ARA, ARIANNA, and RNO-G—and planned—IceCube-Gen2. So far, their ability to measure neutrino flavor had remained unexplored. We show and quantify how the neutrino flavor can be measured with in-ice radio detectors using two complementary detection channels. The first channel, sensitive to ν_e , identifies them via their charged-current interactions, whose radio emission is elongated in time due to the Landau-Pomeranchuk-Migdal effect. The second channel, sensitive to ν_μ and ν_τ , identifies events made up of multiple showers generated by the muons and taus they generate. We show this in state-of-the-art forecasts geared at IceCube-Gen2, for representative choices of the UHE neutrino flux. This newfound sensitivity could allow us to infer the UHE neutrino flavor composition at their sources—and thus the neutrino production mechanism—and to probe UHE neutrino physics.

I. INTRODUCTION

Ultra-high-energy (UHE) cosmic neutrinos, with energies larger than 10^{17} eV, hold vast potential to probe astrophysics and fundamental physics at the highest energies. They were first predicted more than fifty years ago [1], as byproducts of the interaction of ultra-high-energy cosmic rays (UHECRs) with the cosmic microwave background [2, 3]. However, because their flux is low, they have eluded detection so far [4, 5]. Soon, though, a new generation of large-scale UHE neutrino telescopes [6–9], presently in different stages of planning, construction, and prototyping, could finally discover them, realizing long-awaited opportunities.

Measurement of the flavor composition of UHE neutrinos—i.e., the proportion of ν_e , ν_μ , and ν_τ in their flux—represents one such opportunity, one with the power to deliver remarkably versatile insight. For astrophysics, the flavor composition reflects the physical conditions present inside the astrophysical neutrino sources and so may hint at their identity, which so far remains unknown [12–35]. For fundamental physics, it probes the standard paradigm of neutrino oscillations and may reveal physics beyond the Standard Model [6, 12, 13, 17, 18, 21, 23–25, 34, 36–70]. At TeV–PeV neutrino energies, the IceCube neutrino telescope regularly measures the flavor composition of high-energy cosmic neutrinos [71–77]. However, at ultra-high energies, the measurement of the neutrino flavor composition is largely unexplored. In the following, we address this shortcoming.

In-ice radio-detection [9] is a promising and mature technique for measuring UHE neutrinos. Neutrino detectors that adopt it consist of compact detector stations made up of a handful of antennas, deployed in polar ice sheets at shallow depths. They search for nanosecond-long radio flashes, known as Askaryan radiation [78], gen-

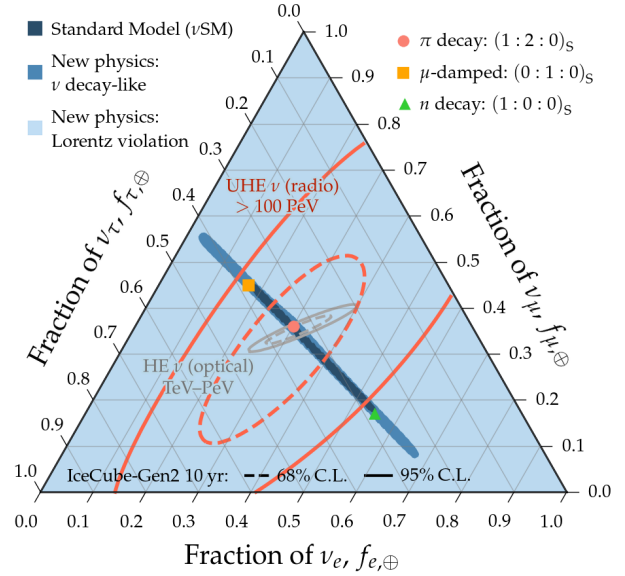


FIG. 1. *Measurement forecasts of the flavor composition of the diffuse flux of ultra-high-energy (UHE, $\gtrsim 100$ PeV) cosmic neutrinos.* We show the first forecasts of flavor measurements via neutrino radio-detection, geared at the planned radio array of IceCube-Gen2 [10]. For comparison, we show also forecasts for high-energy (HE, TeV–PeV) neutrinos, using optical detection in IceCube-Gen2 [11]. In this figure, for illustration, we assume a large benchmark UHE neutrino flux (Fig. 7) produced in pion decays. Our results are based on state-of-the-art simulations of in-ice neutrino radio-detection. The predicted regions of allowed flavor composition at Earth [12], under standard oscillations and new physics, use narrow ranges of the neutrino mixing parameters foreseen for 2040 [13]. *Measuring the UHE flavor composition will further our insight into neutrino physics and astrophysics.*

erated by neutrino interactions in the ice. This allows for the cost-efficient instrumentation of huge volumes needed to detect the low flux of UHE neutrinos. The technical feasibility of the technique was demonstrated in the pathfinder arrays RICE, ARA, and ARIANNA at the South Pole and on the Ross Ice Shelf in Antarctica [79–84]. Currently, the Radio Neutrino Observatory in Greenland (RNO-G) is under construction [85] which has the potential to measure the first UHE neutrino. At the same time, an order-of-magnitude more sensitive radio detector is in advanced planning stages as part of IceCube-Gen2 [10, 86, 87]. Depending on the flux of UHE neutrinos, tens to hundreds of them could be observed over the lifetime of IceCube-Gen2 [88–91], providing insight into the origin of UHECRs [92, 93].

Here, for the first time, we forecast the ability to measure the flavor composition of UHE neutrinos at Earth using in-ice radio-detection in a large array like IceCube-Gen2. This work complements the forecasts of the other main science objectives of discovering and characterizing the UHE neutrino flux [90, 91], identifying the sources of UHE neutrinos [89], and measuring the UHE neutrino-nucleon cross section [88, 94]. Our work builds up on the advances in modeling the signatures of UHE neutrinos in radio detectors through the NuRadioMC code [95] and its extension to simulate secondary interactions of muons and taus [96, 97].

We obtain sensitivity to the neutrino flavor through two complementary detection channels, which are described in detail in the next section. First, interference of multiple overlapping showers generated by ν_e charged-current (CC) interactions alters the shape of the radio pulse, which can be detected with a deep neural network. (Preliminary results on this were presented in Refs. [98, 99]). Second, ν_μ and ν_τ can be identified by detecting events containing at least two displaced in-ice showers, from their initial CC interaction or from the stochastic energy losses of the muon or tau that they generate. From the combination of both detection channels, we devise, for the first time, sensitivity to the three neutrino flavors in in-ice radio-detection neutrino telescopes, opening up measurements of the flavor composition to the entire range of high-energy cosmic neutrino energies.

Figure 1 summarizes our results, geared towards radio-detection in IceCube-Gen2, which we simulate in state-of-the-art detail. For an optimistic choice of the UHE neutrino flux, our method affords enough precision to distinguish between competing benchmark alternatives of neutrino production at the 95% confidence level (C.L.) in a baseline 10 years of observation. This sensitivity also allows us to contrast between flavor transitions driven by standard oscillations and new physics at the highest energies, where differences may be more apparent. Our methods and results are novel, timely, and do not require additional detector hardware or capabilities compared to those already envisioned. They rely only on searching for distinct features in detected events.

This paper is organized as follows. In Section II, we

describe the flavor-sensitive detection channels in in-ice radio detectors. In Section III, we introduce a neural network to identify ν_e CC interactions. In Section IV, we describe the generation of mock event samples and present our methods to measure neutrino flavor. In Section V, we apply them to forecast the measurement of the UHE flavor composition in IceCube-Gen2. In Section VI, we discuss the impact of our results on UHE neutrino science. In Section VII, we summarize and conclude.

II. HOW TO MEASURE NEUTRINO FLAVOR WITH IN-ICE RADIO DETECTORS

Obtaining sensitivity to the neutrino flavor at ultra-high energies with in-ice radio detectors is challenging because the neutrino interactions of different flavors produce very similar radio signatures.

At these energies, the most likely interaction channel is neutrino-nucleon deep inelastic scattering (νN DIS) [100–106], where the neutrino scatters off of one of the constituent partons of a proton or neutron—most likely a quark—breaking up the nucleon, N , in the process. The interaction is either neutral-current (NC)—mediated by a Z boson, i.e., $\nu_\alpha + N \rightarrow \nu_\alpha + X$, where $\alpha = e, \mu, \tau$, and X represents final-state hadrons—or CC—mediated by a W boson, i.e., $\nu_\alpha + N \rightarrow l_\alpha + X$. At these energies, the νN DIS cross section is nearly equal for neutrinos of all flavor, and for neutrinos and anti-neutrinos. Final-state charged particles initiate particle showers whose electromagnetic emission—radio, in our case—may be detectable. Flavor sensitivity stems exclusively from CC interactions. Fortunately, because the CC νN DIS cross section is roughly three times larger than the NC cross section, events from which to extract flavor sensitivity are not rare.

In a NC interaction, only the final-state hadrons initiate showers. These *hadronic showers* start with a high content of neutrons and pions, but as they evolve they quickly transfer their energy to electromagnetic showers (EM), made up mostly of electrons, positrons, and photons. The particle-content profile of these showers has a typical length of 15 m, is smooth, increasing monotonically until the maximum is reached and then decreases monotonically, and exhibits little variation between showers; see Fig. 2, bottom right, and the examples in Refs. [9, 95]. As they evolve, the EM showers develop a time-varying excess of negative charge that generates a nanosecond-scale impulsive radio signal—Askaryan emission [78]—which in-ice radio detectors target (Fig. 2). Because in NC interactions the radio emission is solely from the final-state hadrons, all neutrino flavors produce the same event signature and are indistinguishable.

In a CC interaction, both the final-state hadrons and lepton initiate showers. Like before, the hadronic shower triggered by the former does not provide flavor sensitivity. The sensitivity stems from the additional Askaryan radiation generated by the final-state electron, muon, or

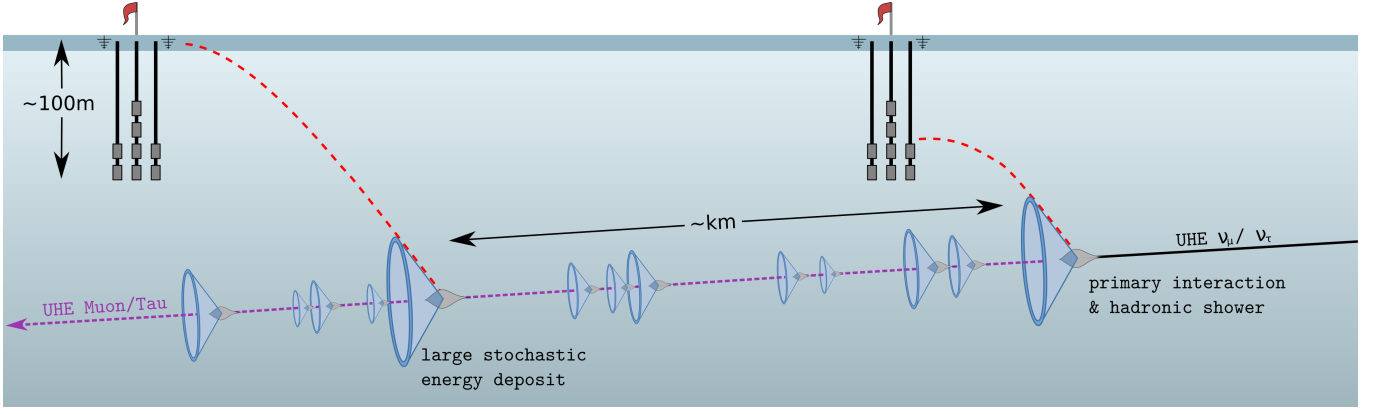


FIG. 2. *Schematic of a charged-current interaction of a UHE ν_μ or ν_τ and its in-ice radio-detection.* The primary neutrino-nucleon interaction produces a hadronic shower. The final-state charged lepton, a muon or a tau, can travel several kilometers while producing sub-showers stochastically, generating Askaryan radiation which can be observed at multiple underground detector stations, resulting in a *multi-shower* event. The change of the index of refraction of radio with depth causes the trajectory of radio signals to bend on their way to the stations, an effect we account for in our simulations. See Section II A for details. *Detecting multi-shower events grants us access primarily to the UHE $\nu_\mu + \nu_\tau$ content (and also, indirectly, to the ν_e content); see Fig. 11.*

tau—depending on whether the interacting neutrino is a ν_e , ν_μ , or ν_τ —whose interactions yield different, distinguishable event signatures. We describe them below.

A. $\nu_\mu + \nu_\tau$ detection channel: radio emission from secondary muons and taus

Figure 2 shows how, in addition to the hadronic shower located at the νN interaction vertex, the muon or tau lepton generated in a CC ν_μ or ν_τ interaction initiates, as it propagates through the ice, several high-energy secondary showers through stochastic energy losses and through decay, in the case of the tau [96]. (The decay length of taus increases roughly linearly with energy and is already approximately 5 km at 10^{17} eV [95], longer than the station spacing considered for IceCube-Gen2. Therefore, tau decays play only a subdominant role at ultra-high energies; see [96] for details.)

These showers are significantly displaced from the νN interaction vertex, on the order of a kilometer. Each shower generates Askaryan emission in the same manner as the hadronic interaction at the νN interaction vertex. This adds additional opportunities for detection, as shown by Ref. [96], increasing the effective detector volume for ν_μ and ν_τ by 20–40% compared to targeting only the radio emission from the νN interaction vertex [96, 97, 107]. The fraction of events with detectable secondary showers for RNO-G [96], IceCube-Gen2 [97], and ARA [107] is similar.

In some events, neighboring detector stations could detect radio emission from the νN interaction and from one of the secondary interactions, which would give a clear and background-free signature of ν_μ and ν_τ [96, 97]. The detection rate of these *multi-shower* events depends on the neutrino energy, the layout of the detector array, the

detector site, and trigger settings. The design parameter with the largest influence on the multi-shower detection rate is the station spacing: the closer neighboring stations are, the higher the probability of multi-shower detection.

Figure 3 shows the expected fraction of CC interactions initiated by ν_μ and ν_τ that are detected as multi-shower

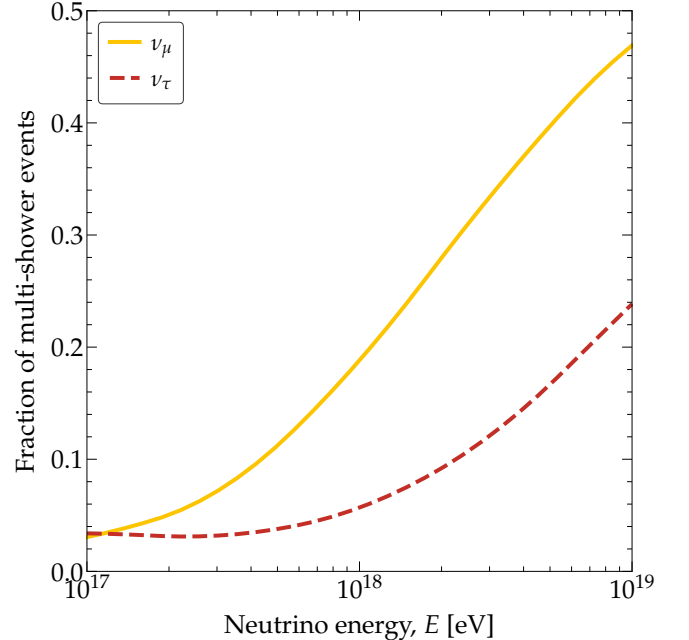


FIG. 3. *Fraction of UHE ν_μ - and ν_τ -initiated CC interactions that can be detected as multi-shower events.* We assume radio-detection in the radio array of IceCube-Gen2 with 2 km spacing between detector stations. Data obtained from the detailed detector simulations of Ref. [97]. See Section II A for details.

events in the radio array of IceCube-Gen2 [97]. Later, we use this fraction in our analysis. The fraction increases with energy, as the probability of large stochastic showers happening increases, and is significantly higher for ν_μ because, statistically, muons deposit larger fractions of their energy. Yet, from a single detected multi-shower event, we do not foresee distinguishing if the interacting neutrino was a ν_μ vs. a ν_τ , but its detection alone rules out that it was a ν_e . In our analysis, the proportion of multi-shower events in a sample of detected events reflects the joint content of $\nu_\mu + \nu_\tau$ in the neutrino flux. Nonetheless, since muons are more likely to trigger multiple stations, there is limited sensitivity separately to the relative abundance of ν_μ and ν_τ (Section V).

Assuming that the direction and position of the showers can be reconstructed sufficiently well, which is supported by current studies [82, 83, 108–114], the only potential background to this detection channel are high-energy muons generated in cosmic-ray-induced air showers. However, their rate of detection by a single station is already low: we expect no more than a handful of events in ten years of operation of IceCube-Gen2 [115], clustered near the low-energy threshold of the experiment, between 10^{16} eV and 10^{17} eV (see also Figs. 3, 4, and 6 in Ref. [90]). Hence, the number of atmospheric muons capable of triggering showers in two neighboring stations is negligible; we ignore it in the following.

B. ν_e detection channel: identification of LPM-elongated showers

Figure 4 shows how, due to the Landau-Pomeranchuk-Migdal (LPM) effect [116–118], ν_e CC interactions can be distinguished from all other neutrino interactions [98, 99, 119, 120]. The LPM effect reduces the bremsstrahlung and pair-production cross sections of the high-energy electron generated in a ν_e CC interaction, as a result of the interference between consecutive scatterings with the medium. This leads to delayed and stochastic shower development with potentially several slightly displaced sub-showers, which, together, elongates the particle profile of the shower and of its radio emission compared to the compact hadronic showers generated in other types of interactions [9, 95]. By identifying this elongation in detected showers, we gain sensitivity to the ν_e content of the neutrino flux, as we explain below.

The magnitude of the LPM effect grows with energy. Below 10^{18} eV, it mostly just delays the start of the electron-induced shower with respect to the hadronic shower. At higher energies, in addition, the electron-induced shower displays more structure and consists of multiple displaced sub-showers; see, e.g., Fig. 4, bottom left, and Ref. [9]. However, despite the shower elongation, the combined hadronic and electromagnetic showers remain small, i.e., a few tens of meters, and so they are detected in superposition by a single station. The interference between two or more spatially separate, but

overlapping or adjacent showers is encoded in the radio waveform recorded by the station [121]. These subtle features in the waveform shape allow us to distinguish events that are initiated by ν_e CC interactions from all other interactions, which in turn allows us to estimate the ν_e fraction in the UHE neutrino flux. Also, pulse shapes generated by the ν_μ and ν_τ CC interactions look like non- ν_e CC interactions as they produce spatially displaced non-overlapping showers (see also the discussion of potential background below).

In our analysis, we use a deep neural network to classify ν_e CC vs. non- ν_e CC events; we describe it in Section III. The classification is not perfect, i.e., showers due to ν_e CC interactions can only be identified on a statistical basis and with limited accuracy, which limits the sensitivity of this detection channel. But, on the other hand, in a flux with equal content of all neutrino flavors, ν_e CC interactions dominate the number of observed events; see Fig. 9 (also, Fig. 14 in Ref. [88]). Later, in Section V, we report that this detection channel provides sensitivity to ν_e similar to the sensitivity to $\nu_\mu + \nu_\tau$ provided by the multi-shower channel. Yet, in contrast, the ν_e CC detection channel has room for improvement. A better classifier would improve the sensitivity to ν_e , whereas the multi-shower detection channel is limited by the underlying physics, i.e., by the probability of large stochastic energy losses of muons and taus.

A background to the ν_e CC detection channel would be any process that generates multiple overlapping showers in the ice whose radio emission interferes with each other, mimicking the interference due to the LPM effect. However, since our classifier is not perfect (Section III), a small background contamination is acceptable and can be quantified and accounted for, statistically. Below, we briefly discuss potential backgrounds.

In the CC interaction of a ν_μ or ν_τ , there is negligible probability that a large shower is initiated by the secondary interaction of a muon or tau close enough to the hadronic shower at the νN interaction vertex for the radio emission from both interactions to interfere and mimic the waveform of a ν_e CC interaction; cf. Refs. [96, 97]. Still, such secondary interaction—or decay, in the case of a tau (see below)—can initiate an EM shower. Yet, as this is only a single EM shower—as opposed to ν_e CC interactions, where there is an additional hadronic shower with which to interfere—its energy would need to be fairly high for it to exhibit the substructure, i.e., multiple slightly-displaced sub-showers, that would set it apart from a hadronic shower and lead it to being incorrectly classified as coming from a ν_e CC interaction. Thus, this represents a background only if the initial neutrino interaction was not also observed. Hence, the potential background is the small fraction of high-energy EM showers induced by the already rare muons or taus whose secondary interactions are detected but whose primary interactions are missed. Therefore, the background to ν_e CC interactions from secondary muon and tau interactions is small; we will ignore it in the fol-

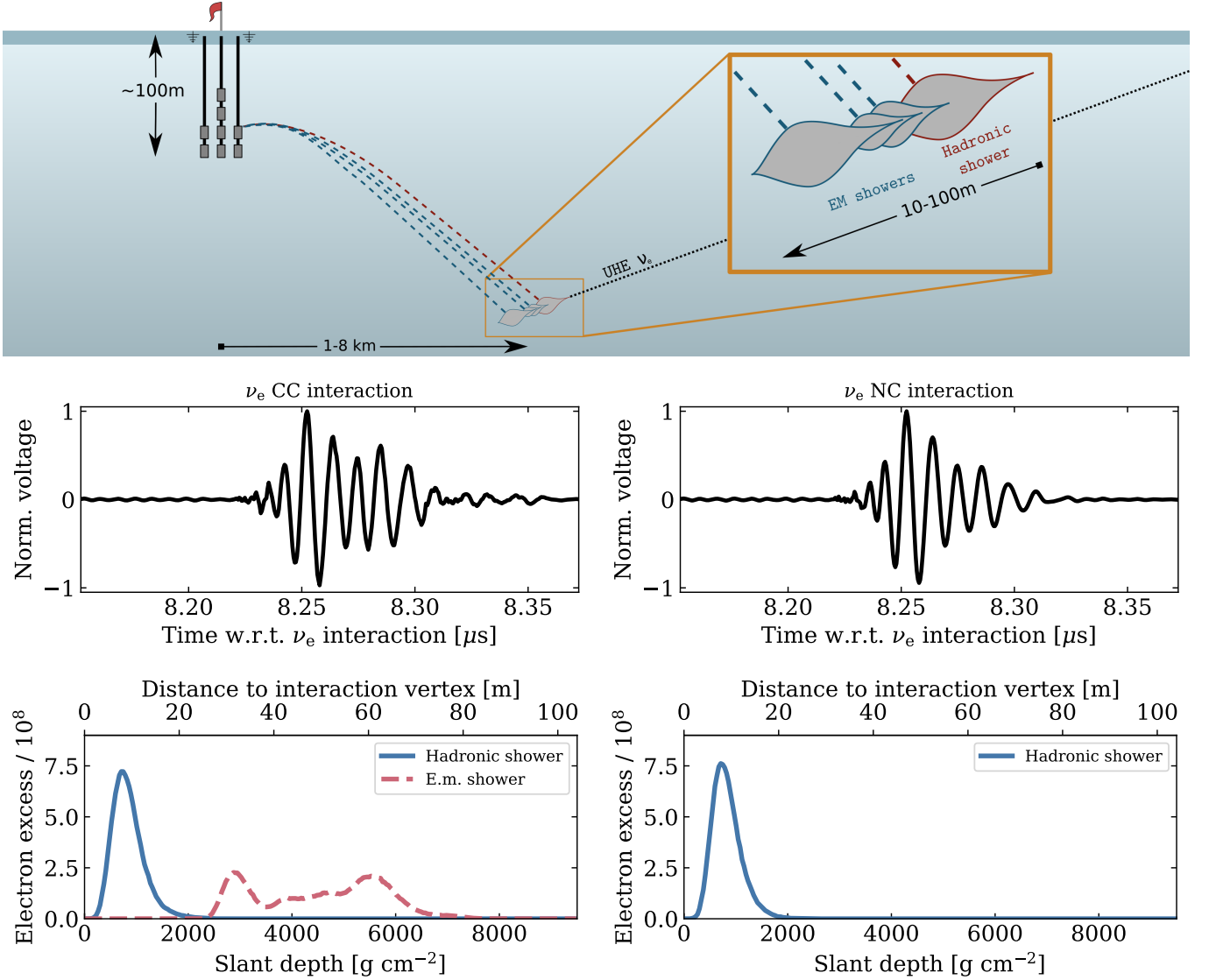


FIG. 4. *Schematic of a charged-current interaction of a UHE ν_e and its in-ice radio-detection.* *Top:* The primary neutrino-nucleon interaction produces a hadronic shower. The final-state electron is affected by the LPM effect, resulting in multiple, separated electromagnetic (EM) sub-showers that imprint on the voltage waveform recorded by the detector stations. The change of the index of refraction of radio with depth causes the trajectory of radio signals to bend on their way to the stations, an effect we account for in our simulations. *Center:* Normalized noiseless voltage waveforms recorded in a detector antenna (an LPDA) triggered by a 3-EeV ν_e undergoing a CC (left) or NC (right) interaction, with otherwise identical initial conditions. The additional late-time large-amplitude “wiggles” in the CC case, compared to the NC case, are due to the sub-showers induced by the LPM effect. We build a custom convolutional neural network to identify their presence (Section III). *Bottom:* Electron excess profiles as a function of the slant depth and geometric distance corresponding to the waveforms shown in the central panels, showing separately the contributions of the hadronic and electromagnetic showers. See Section II B for details. *Identifying ν_e CC events grants us access primarily to the UHE ν_e content; see Fig. 11.*

lowing.

Regarding tau decays, they are only a relevant contribution to the detection rate up to approximately $5 \cdot 10^{17}$ eV, since higher-energy taus are too long-lived to decay inside the detector array, and only 18% of those that do produce an electron [122]. Therefore, the background to ν_e CC interactions from tau decays is also small and we will ignore it.

C. Additional detection channels

In the following, we briefly describe alternative detection channels that offer flavor sensitivity. We do not explore them here, but they are explored elsewhere or might be explored in the future.

Tau regeneration through the Earth: The Earth is opaque to UHE neutrinos, but UHE ν_τ can

TABLE I. *Topology of the neural network used to distinguish waveforms that are produced via showers influenced by the LPM effect.* The size of the data in the (antenna, time, layer) dimensions, where applicable, are given along with the total number of trainable parameters for each block or layer. See Section III B for details.

Network component	Size of the output data	Kernel size	Number of filters	Trainable parameters
Convolution block 1	(5, 512, 32)	5	32	20 800
Convolution block 2	(5, 128, 64)	5	64	71 936
Convolution block 3	(5, 32, 128)	5	128	287 232
Convolution block 4	(5, 8, 256)	5	256	1 147 904
Dense layer 1	512	1 311 232
Dense layer 2	512	262 656
Dense layer 3	1	1 026

propagate greater distances due to tau regeneration [123, 124]. The short lifetime of the tau causes it to decay back into a neutrino before losing a large fraction of its initial energy to the medium. This process can repeat several times, allowing ν_τ to propagate farther through the Earth than ν_e and ν_μ , but losing energy during this process. Therefore, a part of the ν_τ flux at ultra-high energies is converted to a flux with energies two-to-three orders of magnitude lower, depending on the arrival direction to the detector [88, 125–127]; most are expected to arrive from directions close to the horizon. Hence, the detection of Earth-traversing neutrinos provides a unique signature for ν_τ . However, the additional event rate from tau regeneration is small. Even for the huge in-ice radio detector foreseen for IceCube-Gen2, we expect less than one detectable event from tau regeneration in ten years of operation [88, 128]. Therefore, we do not consider this detection channel in this work as it would not add additional sensitivity compared to the other two detection channels described above. A search for Earth-traversing neutrinos with optical neutrino telescopes might be more promising [129].

Angular distribution of neutrinos: Reference [130] proposed to infer the flavor composition of UHE neutrinos from the directional distribution of detected events. Different neutrino flavors have slightly different angular distributions, primarily because the probability of detecting a secondary interaction from muons and taus is highest for horizontal directions, which allows the lepton to propagate through more ice, thereby increasing the chance of undergoing a stochastic energy loss observed by a radio detector station. The work of reference [130] from 10 years ago showed promising results, but is now dated, since it used overly optimistic neutrino flux models and fairly simplistic simulation codes compared to present-day standards, so that the results are not directly comparable to our work. It would be interesting to reassess this observable using, e.g., the state-of-the-art lepton propagation code PROPOSAL [131] and its inte-

gration into NuRadioMC [96], on which our work is based.

Combination of detection techniques: The all-flavor neutrino energy spectrum measured with in-ice radio detectors can be combined with the measurement of air-shower detectors, which are only sensitive to ν_τ , to gain sensitivity to the ν_τ content. However, the method requires the existence of two large UHE neutrino telescopes, which adds another layer of challenge. A potential future option would be the combination of measurements by IceCube-Gen2—all-flavor—and GRAND—only ν_τ —as studied in Ref. [132].

III. IDENTIFICATION OF ν_e CC INTERACTIONS USING A NEURAL NETWORK

As described above, the LPM effect imprints characteristic features in neutrino-induced in-ice radio waveforms that allow us to identify UHE ν_e CC events. We developed a neural network that identifies these features, which we use to infer the fraction of ν_e in the flux of UHE neutrinos.

A. Simulated data

To train the network, we simulated the radio emission from in-ice cascades in the South Pole ice using NuRadioMC [95–97, 108]. Training was carried out for *shallow stations* as pioneered by ARIANNA [80], i.e., detector stations made up of four log-periodic dipole array (LPDA) antennas and one vertically polarized dipole antenna, buried a few meters in the ice. The configuration and trigger settings are the same as foreseen for IceCube-Gen2 [86, 87] and include a full trigger simulation in the presence of thermal noise. The simulations are identical to those in Ref. [111]; details can be found therein.

The current baseline design for IceCube-Gen2 consists of a hybrid array of *shallow* and *deep* station components; a deep component comprises antennas buried up to a depth of 150 m installed in three narrow boreholes [87]. In

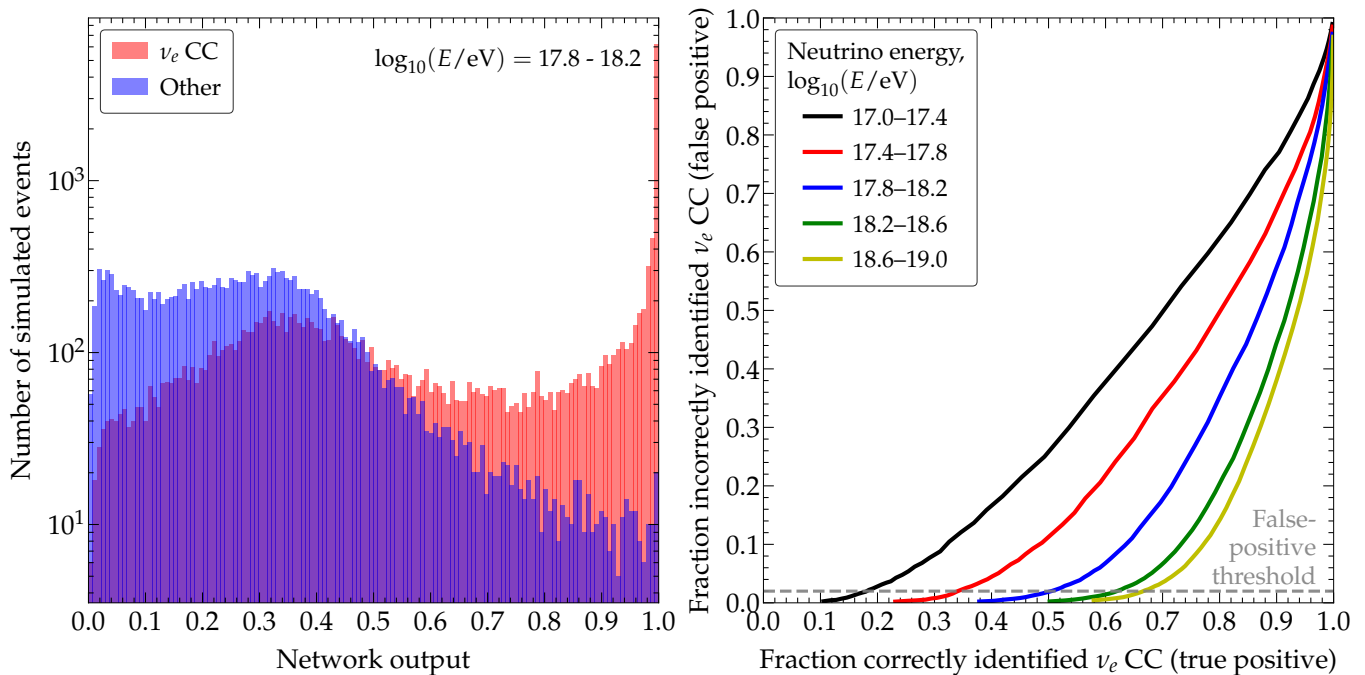


FIG. 5. *Performance of the neural network in classifying ν_e CC events on a test data set.* Left: Network output of the final dense layer for ν_e CC interactions and other interactions in the test data set, for one illustrative energy bin. Right: True-positive and false-positive fractions for the identification of simulated ν_e CC interactions, for different energy bins. The chosen false-positive rate for this analysis is 2%. See Section III for details. The classification is better at higher energies, where $> 65\%$ of ν_e CC events are correctly identified.

the following, we will assume that the results for shallow stations are representative for the entire IceCube-Gen2 array. The ν_e CC sensitivity comes from the pulse shape, which we expect to be measured similarly well with deep detector components. As it may be more than ten years until the measurement we propose here can be conducted, and because in that time the final layout of IceCube-Gen2 is likely to evolve, we forego detailed studies of the impact of the array layout on the flavor sensitivity for now.

To train the network, we simulated ν_e with equal numbers of CC and NC interactions, for neutrino energies from 10^{17} eV to 10^{19} eV, which yield a representative sample of the two different event morphologies that the network aims to classify: ν_e CC and non- ν_e CC.

B. Neural network topology

Table I summarizes the layout of the convolutional neural network (CNN) that we trained on the simulated data described in Section III A to distinguish ν_e CC interactions from all other interactions. The network takes as input the raw waveforms from the four LPDAs and the shallow vertical dipole antenna, sampled at 2 Gsamples s^{-1} , resulting in 512 samples, each lasting 256 ns. The encoding is performed using four blocks of convolutions. Each block consists of four convolutional layers followed by a max-pooling layer. Between each block, the

max-pooling decreases the size of the time dimension by a factor of four while the number of convolutional filters increases by a factor of two such that the overall size of the data decreases after each block.

During the convolution steps, a sliding kernel with five trainable weights is used to perform the convolution operation. Each antenna is treated independently—i.e., the convolution is one-dimensional, applied only to one antenna at a time—and the kernel weights are shared across the antennas. The output is then run through three fully connected—or *dense*—layers. Ultimately, the CNN outputs a classification value for the event. This architecture was inspired by the Visual Geometry Group (VGG) architecture [136] and is motivated by the ability of convolution layers to efficiently analyze pulse shapes. A series of convolution layers with pooling in-between allows modeling more and more complex features. Variants of this architecture have been successfully used for the reconstruction of the neutrino direction and energy of UHE neutrinos [111, 114], and for a low-level trigger [137, 138]. Reference [98] contains further details about the CNN and how we arrived at this architecture.

Figure 5 shows how the trained network performs on an independent test data set. We show the network output for ν_e -CC and non- ν_e -CC interactions with neutrino energies between $10^{17.8}$ eV and $10^{18.2}$ eV. The two distributions are distinct, but partially overlap. By choosing a threshold value for the network output, we can opti-

mize the true-positive rate, i.e., the fraction of correctly identified ν_e CC events, against the false-positive rate, i.e., the fraction of ν_e NC events that contaminate the data set. We found that flavor sensitivity is best when the false-positive rate is low, of a few percent.

Figure 5 right shows the resulting joint distributions of true-positive and false-positive classified events, for all the energy bins used in our analysis (more on this in Section IV C). The discrimination power of the network is indicated by how closely the distribution is to the bottom-right corner, i.e., to most ν_e CC events being correctly classified with the least contamination from NC interactions. The network performs better at higher energies, since the intensity of the LPM effect increases with energy. Further, the average signal-to-noise ratio also increases with energy, meaning that the shape of the radio pulse is less affected by thermal fluctuations. We impose a threshold on the network output such that the false-positive rate is 2% in each of the energy bins. This sets the true-positive rate of the network to roughly 10%–65%, depending on the neutrino energy.

Figure 6 shows the resulting fractions of true-positive and false-positive classifications of our CNN as functions of the neutrino energy. Because the ratio of CC to NC interactions is about 70%, above $10^{18.5}$ eV half of all ν_e interactions are correctly identified as such.

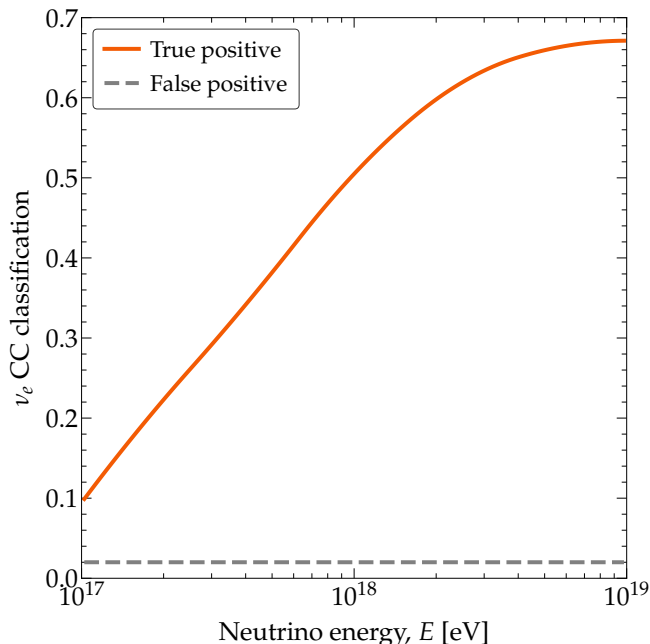


FIG. 6. *True and false positive rates of our convolutional neural network to classify UHE ν_e CC events.* We choose the threshold on the network output such that the false-positive rate is 2%, which we found optimizes flavor identification. See Section III for details.

IV. UHE NEUTRINOS: PREDICTIONS AND DETECTION

Using the techniques described above, we predict the sensitivity of IceCube-Gen2 to the flavor composition of UHE neutrinos. We make projections for two plausible choices of the neutrino flux—a high, optimistic one and a low, pessimistic one—and for three different benchmark choices of the flavor composition. In the following, we describe these choices, the methods that we use to compute the rate of detected events in IceCube-Gen2, and our statistical methods.

A. The all-flavor UHE neutrino flux

The diffuse UHE neutrino flux is unmeasured, but there are multiple theoretical predictions of it; see, e.g., Refs. [141–147] for examples and Ref. [88, 90] for an overview. The models are for cosmogenic neutrinos, produced in UHECR interactions on cosmological photon backgrounds during their propagation—i.e., the cosmic microwave background and the extragalactic background light—for source neutrinos, produced in UHECR interactions with matter and radiation in their sources, or for combinations of both.

For our forecasts, it makes little difference what the origin of the UHE neutrino flux is; rather, what matters is the neutrino energy distribution. Among the theory predictions, the neutrino energy spectrum varies significantly in size and shape, which is partially why planning for its discovery has been challenging; see, e.g., Fig. 2 in Ref. [90]. Still, the predicted energy spectra share a few common features: most of them consist, roughly, of the superposition of a power-law in neutrino energy, especially towards lower energies, and a bump-like spectrum whose width and position vary depending on the model. In some models, the power-law comes from neutrino production via proton-proton interactions, and the bump, from production via proton-photon interactions. Below, we adopt two benchmark UHE neutrino flux models that exhibit these features, which are well motivated, and that are representative of the wide breadth of predictions.

Figure 7 shows our two benchmark UHE neutrino flux models. Each benchmark contains two flux components.

The first flux component is based on the neutrino flux inferred from TeV–PeV through-going muon tracks detected over 9.5 years by IceCube [135]. In this energy range, the $\nu_\mu + \bar{\nu}_\mu$ spectrum is described by a power law $\propto E^{-2.37}$. We extrapolate it to ultra-high energies without changes to the shape of its energy spectrum, and multiply it by a factor of 3 to convert it to an all-flavor flux, under the nominal assumption that neutrinos of all flavors are equally abundant (Section IV B). Later, we redistribute the all-flavor flux among different flavors using different assumptions of the flavor composition. We include this flux component to account for the possibility that the TeV–PeV neutrino flux extends to higher en-

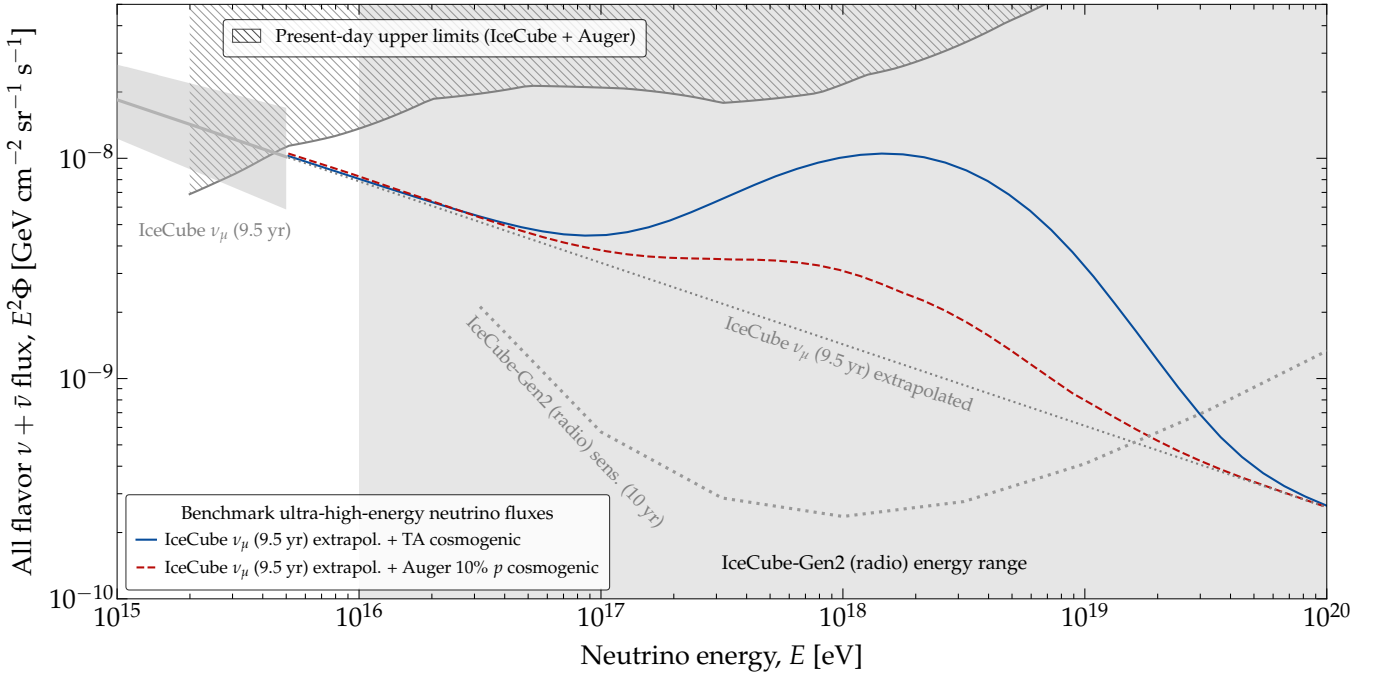


FIG. 7. **Benchmark models of the UHE neutrino flux.** Our optimistic benchmark flux is built from the cosmogenic flux derived from fits to UHECR data from the Telescope Array (TA) [133]; our pessimistic one, from the cosmogenic flux derived from fits to UHECR data from the Pierre Auger Observatory (Auger), assuming that 10% of the cosmic rays are protons [134]. To each, we add the IceCube flux derived from 9.5 years of through-going tracks [135] (“IceCube ν_μ (9.5 yr)”), extrapolated to ultra-high energies. The projected sensitivity of the radio array of IceCube-Gen2 is from Ref. [86]. Present-day upper limits on the flux of UHE neutrinos are from IceCube [4] and Auger [5]. See Section IV A for details. *Our benchmark flux models are representative of the breadth of theoretical flux predictions.*

TABLE II. **Benchmark scenarios of UHE neutrino flavor composition used in our forecasts.** For each neutrino flavor, $f_{\alpha,S}$ is the ratio of $\nu_\alpha + \bar{\nu}_\alpha$ ($\alpha = e, \mu, \tau$) to the all-flavor neutrino flux emitted at the source. After oscillations en route to Earth, the flavor composition is transformed into $f_{\alpha,\oplus}$. We compute the latter assuming the present-day best-fit values of the neutrino mixing parameters from NuFit 5.2 [139, 140]. See Section IV B for details.

Benchmark neutrino production	UHE neutrino flavor composition	
	At sources, $(f_{e,S}, f_{\mu,S}, f_{\tau,S})$	At Earth, $(f_{e,\oplus}, f_{\mu,\oplus}, f_{\tau,\oplus})$
Pion decay	$(\frac{1}{3}, \frac{2}{3}, 0)$	(0.30, 0.36, 0.34)
Muon-damped	(0, 1, 0)	(0.17, 0.45, 0.37)
Neutron decay	(1, 0, 0)	(0.55, 0.17, 0.28)

ergies. This component yields 30–35 detected neutrinos over ten years, depending on its flavor composition.

The second flux component is a prediction of the cosmogenic neutrino flux, inferred from fits to the measured UHECR spectrum and mass composition. This is the dominant component at ultra-high energies. To build our benchmark fluxes, we consider two alternatives. Our optimistic benchmark uses the cosmogenic flux derived from fits to UHECR data from the Telescope Array (TA) [133]; our pessimistic one, the cosmogenic flux derived from fits to UHECR data from the Pierre Auger Observatory (Auger), assuming that 10% of the cosmic rays are protons [134]. While the original construction of these flux models included predictions of the energy-dependent fla-

vor composition at Earth, for our analysis we use only the all-flavor flux. Later, we re-distribute it among different flavors using different assumptions of the flavor composition. This flux component yields 139–164 detected neutrinos over ten years for the high benchmark and 23–28 neutrinos for the low one, depending on their flavor composition.

B. The UHE neutrino flavor composition

Table II summarizes the three benchmark choices of the UHE neutrino flavor composition that we adopt to make our forecasts of flavor measurement. There are

other possibilities for the flavor composition with which neutrinos can be produced, including changes with neutrino energy (see, e.g., Refs. [33, 45, 148] and Section VI), but we take these three as benchmarks, constant across the energies that we consider. Below, we expand on them.

The interactions of UHECRs with matter and radiation produce high-energy pions that, upon decaying, produce high-energy neutrinos, i.e., $\pi^+ \rightarrow \mu^+ + \nu_\mu$, followed by $\mu^+ \rightarrow e^+ + \nu_e + \bar{\nu}_\mu$, and their charged-conjugated processes. Thus, the full pion decay chain yields a flavor composition at the neutrino sources (S) of $(f_{e,S}, f_{\mu,S}, f_{\tau,S}) = (\frac{1}{3}, \frac{2}{3}, 0)$, where $f_{\alpha,S}$ is the ratio of $\nu_\alpha + \bar{\nu}_\alpha$ to the all-flavor neutrino yield ($\alpha = e, \mu, \tau$). We do not separate ν_α from $\bar{\nu}_\alpha$ because high-energy neutrino telescopes presently cannot distinguish between them. In sources that harbor intense magnetic fields, the intermediate muons might cool via synchrotron radiation, so that the only high-energy neutrinos emitted are directly from the decay of pions; in this case, the flavor composition is $(0, 1, 0)_S$. Separately, the beta-decay of neutrons and neutron-rich isotopes produces a pure- $\bar{\nu}_e$ flux; in this case, the flavor composition is $(1, 0, 0)_S$.

En route to Earth (\oplus), neutrino oscillations modify the flavor composition into $f_{\alpha,\oplus} = \sum_{\beta=e,\mu,\tau} P_{\beta\alpha} f_{\beta,S}$, where $P_{\beta\alpha} = \sum_{i=1}^3 |U_{\beta i}|^2 |U_{\alpha i}|^2$ is the average flavor-transition probability and U is the Pontecorvo-Maki-Nakagawa-Sakata mixing matrix. The latter depends on the neutrino mixing parameters θ_{12} , θ_{23} , θ_{13} , and δ_{CP} . Table II shows the flavor composition at Earth for our three benchmark cases, computed using the present-day best-fit values of the mixing parameters. Production by pion decay yields close to flavor equipartition at Earth; this is the nominal expectation.

Today, the uncertainty in the mixing parameters is sizable and impacts the prediction of the allowed neutrino flavor composition at Earth [12, 13, 148]. However, in the years 2030–2040, the mixing angles should be known to within 1% of their values and the CP violation phase should be known to within a few percent of its value, thanks to measurements by upcoming oscillation experiments DUNE, Hyper-Kamiokande, and JUNO. At that point, the impact of the uncertainties in the mixing parameters on the predicted flavor composition at Earth should be tiny [13]. Therefore, in our forecasts below, we neglect the uncertainty in the mixing parameters, and fix them to their present-day best-fit values from the NuFit 5.2 global fit to oscillation data [139, 140].

C. Generating samples of detected events

To generate measurement forecasts of the UHE neutrino flavor composition, we generate mock samples of events detected by a radio array based on the IceCube-Gen2 design [87]. To do this, we estimate the response of the detector via its simulated effective volume.

Figure 8 shows the effective volumes that we use. They are calculated using NuRadioMC [95, 108], using

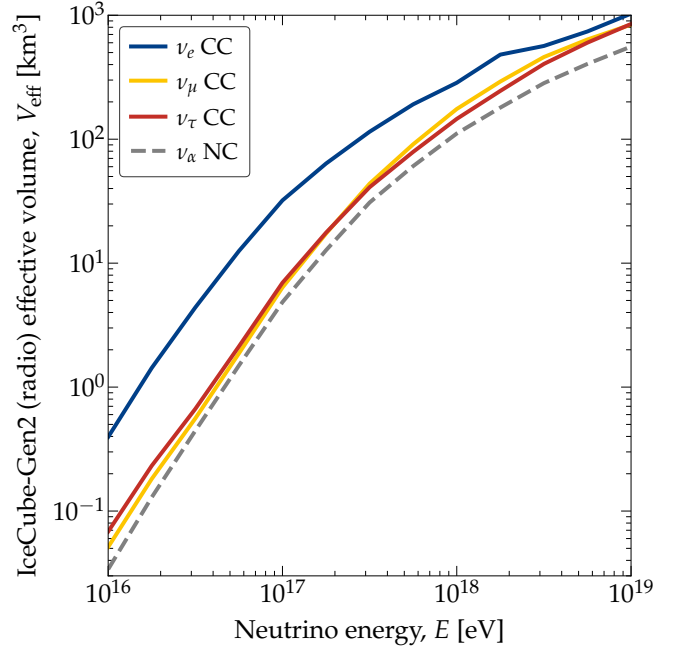


FIG. 8. *Effective volume for UHE neutrino detection in the radio array of IceCube-Gen2.* We treat separately CC interactions of ν_e , ν_μ , and ν_τ , and NC interactions of all neutrino flavors. See Section IV C for details.

the same settings as for other IceCube-Gen2 studies; see Refs. [86, 87] for details. The effective volumes are direction-averaged and include the effect of the attenuation of the neutrino flux while propagating inside the Earth, i.e., the probability of a neutrino reaching the simulation volume. We approximate the effective volume of the full detector by multiplying the effective volume of a single shallow detector station and a single deep detector station by the respective number of shallow and deep stations foreseen in the IceCube-Gen2 radio array, as was done in previous studies that forecast its science potential; e.g., Refs. [88–91]). Doing this slightly overestimates the effective volume at the highest energies, since in reality a fraction of νN interactions is expected to be detected by multiple stations. This fraction depends on the station spacing. The design goal of IceCube-Gen2 is to keep the fraction at about 10% at 10^{18} eV [87]. We ignore this correction in the following.

We calculate the effective volume separately for ν_e CC and NC interactions. Then we use the results of Ref. [97] to increase the ν_μ and ν_τ CC effective volumes by accounting for the observation of showers produced by the muons and taus. The NC effective volumes of all flavors are the same. Because in ν_e CC interactions the entire neutrino energy is converted into electromagnetic energy, the effective volume for ν_e CC interactions dominates over all other channels; e.g., at 10^{17} eV, it is larger than the other channels by a factor of about 5.

Using the above effective volumes, V_α^{CC} and V_α^{NC} , we compute the effective areas, $A_\alpha^{CC} \equiv V_\alpha^{CC}/\lambda_\alpha^{CC}$ and

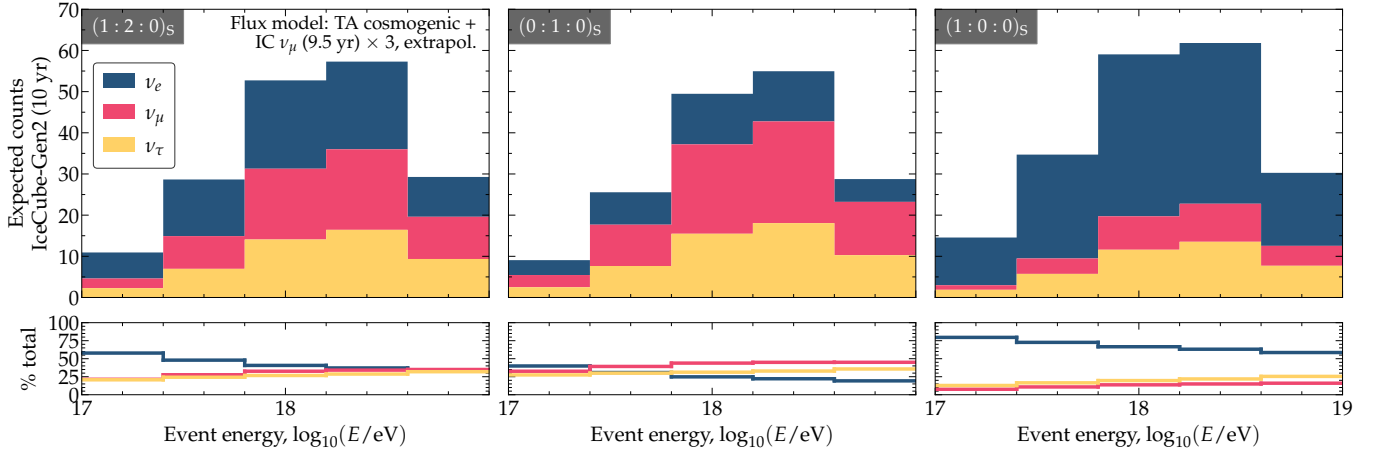


FIG. 9. *Mean expected number of detected events in the radio array of IceCube-Gen2, showing contributions of each neutrino flavor.* For this figure (also Fig. 10), we assume our high UHE neutrino benchmark flux model, which uses the cosmogenic neutrino prediction based on TA UHECR data (Fig. 7). To produce our forecasts, we also compute the spectrum assuming our lower UHE neutrino benchmark flux model (not shown here). *Left:* Assuming the production of UHE neutrinos from the decay of pions at the sources, $(1/3, 2/3, 0)_S$, which yields $(0.30, 0.36, 0.34)_\oplus$ at Earth. *Center:* Assuming muon-damped flavor composition at the sources, $(0, 1, 0)_S$, which yields $(0.17, 0.45, 0.37)_\oplus$. *Right:* Assuming neutrino production via neutron decay at the sources, $(1, 0, 0)_S$, which yields $(0.55, 0.17, 0.28)_\oplus$. See Section IV C for details.

$A_\alpha^{\text{NC}} \equiv V_\alpha^{\text{NC}}/\lambda_\alpha^{\text{NC}}$, where $\lambda_\alpha^{\text{CC}} \equiv (\sigma_{\nu N}^{\text{CC}} n_N)^{-1}$ is the neutrino CC interaction length in ice, $\sigma_{\nu N}^{\text{CC}}$ is the νN CC cross section and n_N is the number density of nucleons in ice, and similarly for NC. At these energies, the CC cross section of ν_α and $\bar{\nu}_\alpha$ of all flavors are nearly equal, and the same holds for NC. Thus, for a given choice of all-flavor UHE neutrino flux, $\Phi_{\nu_{\text{all}}}$, and of the flavor composition at Earth, $f_{\alpha,\oplus}$, from among our benchmarks (Section IV A and IV B), the mean differential number of detected events due to $\nu_\alpha + \bar{\nu}_\alpha$ CC interactions, after an observation time T , is

$$\frac{dN_{\nu_\alpha}^{\text{CC}}}{dE} = 4\pi T f_{\alpha,\oplus} \Phi_{\nu_{\text{all}}}(E) A_\alpha^{\text{CC}}(E), \quad (1)$$

and similarly for NC, with $\text{CC} \rightarrow \text{NC}$. The factor of 4π in Eq. (1) accounts for integration over the full sky. We integrate Eq. (1), and its NC counterpart, in energy to compute the event rates in $N_E = 5$ energy bins between 10^{17} eV and 10^{19} eV, evenly spaced in logarithmic scale, i.e., $N_{\nu_\alpha,i}^{\text{CC}}$ and $N_{\nu_\alpha,i}^{\text{NC}}$ in the i -th bin. The energy range in this analysis is selected by the overlap of where the CNN was trained and where the data to define the effective area was available. This energy range also contains the bulk of the expected events for the benchmark flux models, which drive the sensitivity to the flavor. Our main forecasts are for $T = 10$ years of detector exposure. Later, as part of our statistical analysis (Sections VB to VD), we account for statistical fluctuations in the number of detected events by using the mean event rate as the central value of a Poisson distribution.

Figure 9 shows the contribution of the different neutrino flavors to the mean energy spectrum of events, for our three benchmark choices of flavor composition. The event rate is highest between 10^{18} eV and $10^{18.6}$ eV be-

cause this is where our benchmark UHE neutrino flux peaks (Fig. 7). At lower energies, the effective volume is small; at higher energies, the flux is low. Under approximate flavor equipartition at Earth, i.e., the pion-decay model with $(1/3, 2/3, 0)_S$ and $(0.30, 0.36, 0.34)_\oplus$, the dominant contribution is from ν_e , since its effective volume is the largest (Fig. 8). For other choices of the flavor composition, the contribution of the different flavors reflects the underlying flavor composition.

We compute three event energy spectra, or observables, that we use in our analysis below:

1. **Total event spectrum, $N_{\nu_{\text{all}},i}$:** This is the number of events due to the CC plus NC interactions of ν_e , ν_μ , and ν_τ , i.e., $N_{\nu_{\text{all}},i} = N_{\nu_e,i}^{\text{CC}} + N_{\nu_\mu,i}^{\text{CC}} + N_{\nu_\tau,i}^{\text{CC}} + (\text{CC} \rightarrow \text{NC})$. It does not separate flavors.
2. **Spectrum of identified ν_e CC events, $N_{\text{ML},i}$:** We compute the number of ν_e CC events identified by the CNN, $N_{\text{ML},i}$ (“ML” refers to “machine learning”), by adding together a randomly chosen subset of the number of ν_e CC events, $N_{\nu_e,i}^{\text{CC}}$, selected according to the true-positive fraction of the CNN (see Figure 5), and a randomly chosen subset of the number of events that are not ν_e CC events, $N_{\nu_{\text{all}},i} - N_{\nu_e,i}^{\text{CC}}$, selected according to the false-positive fraction of the CNN.
3. **Spectrum of multi-shower events, $N_{\text{mult},i}$:** We compute the number of events where two or more showers trigger multiple detector stations, $N_{\text{mult},i}$, by adding together a randomly chosen subset of the number of events triggered by ν_μ CC interactions, $N_{\nu_\mu,i}^{\text{CC}}$, and a randomly chosen subset of

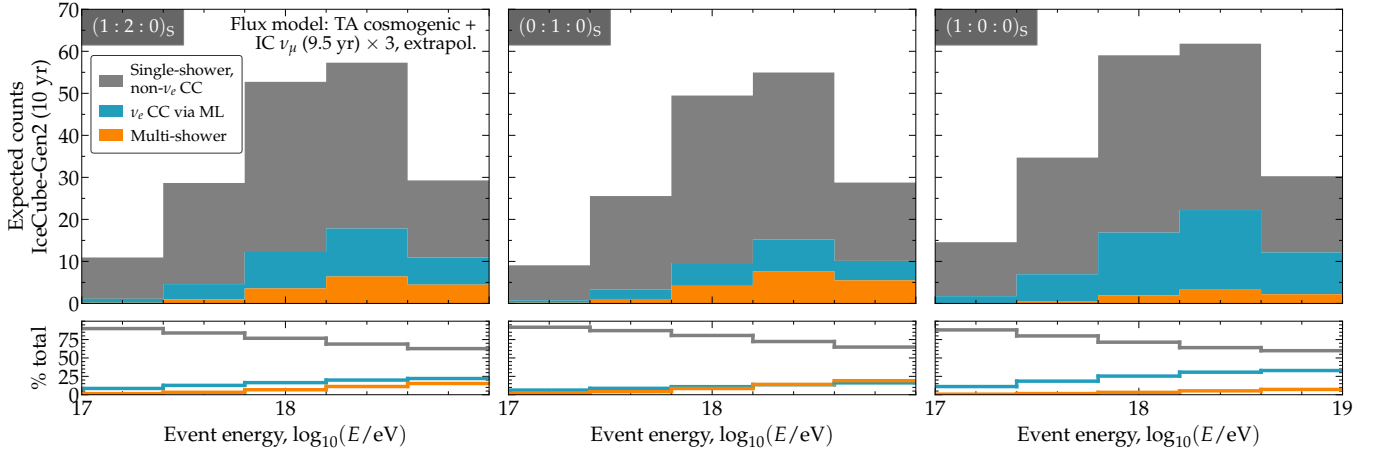


FIG. 10. *Mean expected numbers of observed events, showing contributions of each detection channel.* Same as Fig. 9, but showing instead the contributions of each detection channel: single-station events not classified as ν_e CC, single-station events classified as ν_e CC (Section II B), and multi-shower events (Section II A). See Section IV C for details.

the number of events triggered by ν_τ CC interactions, $N_{\nu_\tau,i}^{\text{CC}}$, based on the expected fraction of multi-shower events (Fig. 3).

Figure 10 shows the above three event spectra. Like for Fig. 9, the overall shape of the event spectra reflects the interplay of the neutrino energy spectrum and the detector effective volume. Our capability to measure the UHE neutrino flavor composition rests on identifying ν_e CC events and multi-shower events. Figure 10 reveals that these events make up less than 25% of the total between 10^{18} eV and $10^{18.6}$ eV, where most of the events lie given our two flux benchmarks. Below, we show that although these events are sub-dominant, they are common enough to grant us the flavor sensitivity that we seek.

V. MEASUREMENT FORECASTS OF THE UHE NEUTRINO FLAVOR COMPOSITION

A. Overview of the statistical analysis

To gauge the flavor sensitivity of the in-ice radio array, first, we generate a mock sample of events assuming one of our benchmark choices of the all-flavor flux (Section IV A) and of the flavor composition (Section IV B). We take this as our observed event sample, consisting of $N_{\nu_{\text{all}},i}^{\text{obs}}$, $N_{\nu_{\text{ML}},i}^{\text{obs}}$, and $N_{\nu_{\text{mult}},i}^{\text{obs}}$ (Section IV C). Second, we perform a hypothesis test to recover from this sample the most likely flavor composition, i.e., $f_{e,\oplus}$, $f_{\mu,\oplus}$, and $f_{\tau,\oplus}$. We do this by comparing, via a likelihood function (defined later), our observed event sample against test event samples computed under varying hypotheses.

Table III shows the free model parameters of our analysis; they describe the all-flavor neutrino energy spectrum and the flavor composition. For the all-flavor energy spectrum, we proceed as in an analysis of real data in which the normalization and shape of the all-flavor

energy spectrum, $\Phi_{\nu_{\text{all}}}$, would be unknown. Thus, we approximate the all-flavor spectrum by a third-order log-log polynomial in neutrino energy, which is able to capture the bump-like shape of our benchmark energy spectra (Fig. 7). It is described by the coefficients a , b , c , and d , whose values we let float in a comparison to the observed sample. (Other parametrizations are possible, though we do not explore them here; see Ref. [71].) For the flavor composition, we let $f_{e,\oplus}$ and $f_{\mu,\oplus}$ float; since $f_{\tau,\oplus} \equiv 1 - f_{e,\oplus} - f_{\mu,\oplus}$, we do not float it separately.

In our analysis, we vary the values of a , b , c , d , $f_{e,\oplus}$, and $f_{\mu,\oplus}$ and, for each realization of them, we generate a test event sample consisting of $N_{\nu_{\text{all}},i}$, $N_{\nu_{\text{ML}},i}$, and $N_{\nu_{\text{mult}},i}$ (Section IV C). We compare the test event sample against our assumed observed sample via a likelihood function (defined below) that accounts for Poisson fluctuations in the number of events. The likelihood is then marginalized with respect to the all-flavor spectrum parameters, and we report measurements on the flavor composition alone.

Below, we apply the procedure outlined above to three sets of observables to achieve sensitivity only to the ν_e content via $N_{\nu_{\text{all}},i}$ plus $N_{\nu_{\text{ML}},i}$ (Section V B), sensitivity only to the $\nu_\mu + \nu_\tau$ content via $N_{\nu_{\text{all}},i}$ plus $N_{\nu_{\text{mult}},i}$ (Section V C), and sensitivity to the three flavors via $N_{\nu_{\text{all}},i}$ plus $N_{\nu_{\text{ML}},i}$ plus $N_{\nu_{\text{mult}},i}$ (Section V D).

B. The ν_e CC channel

For a given test realization of the model parameters, $\theta \equiv (a, b, c, d, f_{e,\oplus}, f_{\mu,\oplus})$ (Table III), the likelihood function that compares the observed *vs.* test events is

$$\mathcal{L}_{\text{ML}}(\theta) = \prod_i^{N_E} \mathcal{P}(N_{\nu_{\text{all}},i}^{\text{obs}}; N_{\nu_{\text{all}},i}(\theta)) P_{\text{ML},i}(\theta), \quad (2)$$

where a Poisson distribution, \mathcal{P} , accounts for the probability of observing $N_{\nu_{\text{all}},i}^{\text{obs}}$ events when the expected num-

TABLE III. *Free model parameters varied in our statistical analysis.* Each parameter floats independently of each other as part of our procedure to infer the UHE flavor composition. See Section V A for details.

Model parameter		Symbol
Physical parameters		
UHE neutrino flavor composition	Electron flavor ratio	$f_{e,\oplus}$
	Muon flavor ratio	$f_{\mu,\oplus}$
Nuisance parameters (profiled over)		
All-flavor UHE neutrino flux, $\log_{10}[\Phi_{\nu_{\text{all}}}/(\text{GeV}^{-1} \text{ cm}^{-2} \text{ s}^{-1} \text{ sr}^{-1})]$ (third-degree polynomial in $x \equiv \log_{10}(E/\text{eV})$)	Coefficient $\propto x^3$	a
	Coefficient $\propto x^2$	b
	Coefficient $\propto x^1$	c
	Coefficient $\propto x^0$	d

ber is $N_{\nu_{\text{all}},i}(\boldsymbol{\theta})$. The term $P_{\text{ML},i}$ accounts for the different ways in which the expected number of true-positive and false-positive events can sum up to $N_{\text{ML},i}^{\text{obs}}$, i.e.,

$$P_{\text{ML},i}(\boldsymbol{\theta}) = \sum_{k=0}^{N_{\text{ML},i}^{\text{obs}}} \mathcal{B}(k; N_{\nu_{\text{all}},i}^{\text{obs}}, p_{\text{tp},i}(\boldsymbol{\theta})) \times \mathcal{B}(N_{\text{ML},i}^{\text{obs}} - k; N_{\nu_{\text{all}},i}^{\text{obs}}, p_{\text{fp},i}(\boldsymbol{\theta})) , \quad (3)$$

where $\mathcal{B}(k; N, p)$ is the binomial probability of observing k out of N events, each having a probability p of being observed. For true-positive (tp) and false-positive (fp) events, the latter is

$$p_{\text{tp},i}(\boldsymbol{\theta}) = \frac{N_{\nu_e,i}^{\text{CC}}(\boldsymbol{\theta})}{N_{\nu_{\text{all}},i}(\boldsymbol{\theta})} \mathcal{T}_i , \quad (4)$$

$$p_{\text{fp},i}(\boldsymbol{\theta}) = \frac{N_{\nu_{\text{all}},i}(\boldsymbol{\theta}) - N_{\nu_e,i}^{\text{CC}}(\boldsymbol{\theta})}{N_{\nu_{\text{all}},i}(\boldsymbol{\theta})} \mathcal{F}_i , \quad (5)$$

where \mathcal{T}_i and \mathcal{F}_i are, respectively, the true-positive and false-positive fractions of events classified by our CNN as being due to a ν_e CC interaction (Fig. 6), averaged in energy inside the i -th bin.

For given values of $f_{e,\oplus}$ and $f_{\mu,\oplus}$, we profile the full likelihood, Eq. (2), by finding the values of the spectrum-shape parameters, a, b, c, d , that maximize it, i.e.,

$$\mathcal{L}_{\text{ML}}(f_{e,\oplus}, f_{\mu,\oplus}) = \max_{a,b,c,d} \mathcal{L}_{\text{ML}}(\boldsymbol{\theta}) . \quad (6)$$

This is the reduced likelihood from which we measure the flavor composition in this channel. We report the best-fit flavor composition and the measurement uncertainties as confidence intervals of $f_{\alpha,\oplus}$, computed using Wilks' theorem. We follow analogous procedures to make forecasts for other detection channels later.

Figure 11 shows the resulting measurement of the flavor composition using ν_e CC events alone, assuming, for illustration, that its true value is that from the full pion decay chain. Naturally, using ν_e CC events alone allows us to measure only $f_{e,\oplus}$. After 10 years of exposure, $f_{e,\oplus}$ could be measured to within 8%, assuming our optimistic UHE neutrino benchmark flux. Fortunately, the theoretically palatable region of predicted flavor composition at Earth [12, 13] (Fig. 1) is aligned nearly orthogonally to

the $f_{e,\oplus}$ axis, so that measuring $f_{e,\oplus}$ affords the greatest sensitivity to distinguish between predictions of the flavor composition at Earth, assuming standard oscillations.

C. The multi-shower channel

Showers triggered by ν_μ and ν_τ CC interactions can be identified due to muons and taus triggering multiple stations due to their stochastic energy losses (Section II A).

In this channel, the observables are the number of NC + CC events of all flavors, $N_{\nu_{\text{all}},i}^{\text{obs}}$, and the number of multi-shower events, $N_{\text{mult},i}^{\text{obs}}$. Together, they provide sensitivity to the three flavors, primarily to ν_e and to the combination of $\nu_\mu + \nu_\tau$. The sensitivity to ν_e comes from the ν_e CC effective volume being larger than for any other detection channel (Fig. 8). The sensitivity to $\nu_\mu + \nu_\tau$ comes from detecting multi-shower events; the degeneracy between ν_μ and ν_τ is only weakly mitigated due to the larger effective volume for ν_μ than ν_τ for the multi-shower channel by about a factor of two (Fig. 3). By combining $N_{\nu_{\text{all}},i}^{\text{obs}}$ with $N_{\text{mult},i}^{\text{obs}}$, the degeneracy between a higher value of $f_{e,\oplus}$ and a lower all-flavor neutrino flux is lifted by the need to also correctly predict the number of multi-shower events.

In analogy with Section V B, the likelihood function is

$$\mathcal{L}_{\text{mult}}(\boldsymbol{\theta}) = \prod_i^{N_E} \mathcal{P}(N_{\nu_{\text{all}},i}^{\text{obs}}; N_{\nu_{\text{all}},i}(\boldsymbol{\theta})) P_{\text{mult},i}(\boldsymbol{\theta}) , \quad (7)$$

where \mathcal{P} is, like before, a Poisson distribution. The probability $P_{\text{mult},i}$ accounts for the different ways in which the contributions of ν_μ and ν_τ to the rate of multi-shower events can sum up to $N_{\text{mult},i}^{\text{obs}}$, i.e.,

$$P_{\text{mult},i}(\boldsymbol{\theta}) = \sum_{k=0}^{N_{\text{mult},i}^{\text{obs}}} \mathcal{B}(k; N_{\nu_{\text{all}},i}^{\text{obs}}, p_{\mu,i}(\boldsymbol{\theta})) \times \mathcal{B}(N_{\text{mult},i}^{\text{obs}} - k; N_{\nu_{\text{all}},i}^{\text{obs}}, p_{\tau,i}(\boldsymbol{\theta})) , \quad (8)$$

where \mathcal{B} is, like before, the binomial distribution, $p_{\mu,i}$ and $p_{\tau,i}$ are, respectively, the probability of a ν_μ and ν_τ

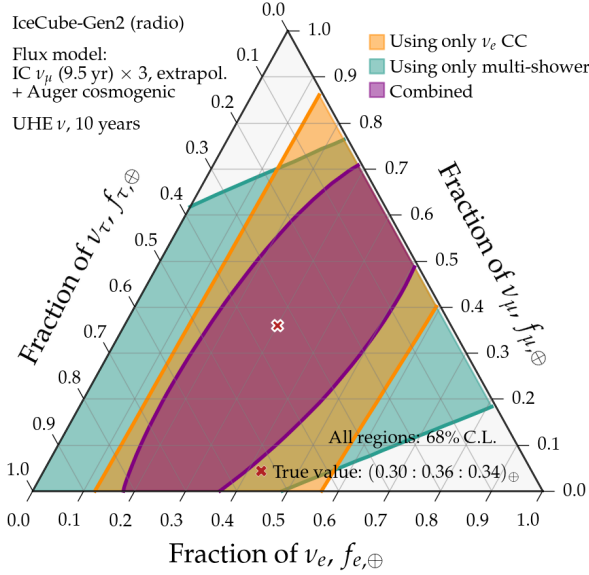
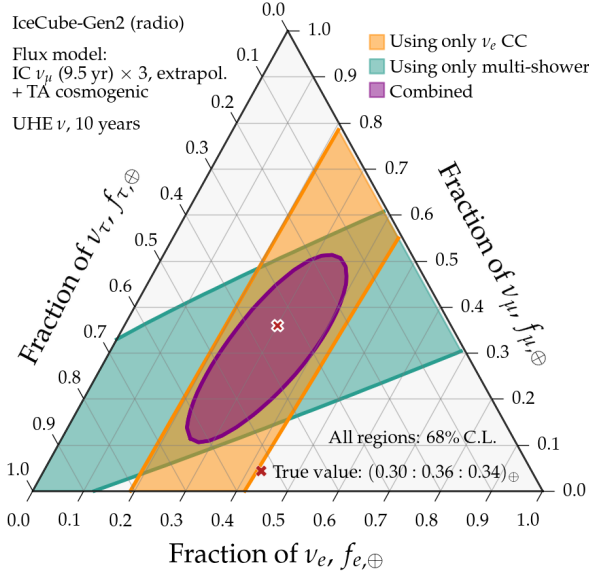


FIG. 11. *Measured flavor composition of the diffuse flux of UHE neutrinos in the radio array of IceCube-Gen2, showing the contributions of the separate flavor-sensitive detection channels.* The regions represent the measurement uncertainty (68% C.L.) assuming neutrino production via pion decay. *Top:* Results assuming our high all-flavor benchmark UHE neutrino flux, obtained from a fit to TA UHECR observations (Fig. 7). *Bottom:* Results assuming our low benchmark flux, obtained from a fit to Auger UHECR observations. See Sections II B and II A for a description of the two detection channels, Fig. 12 for results assuming other benchmarks of flavor composition, and Section V for details. The ν_e CC channel provides sensitivity to the ν_e content; the multi-shower channel provides sensitivity mainly to $\nu_\mu + \nu_\tau$ and also to the ν_e content.

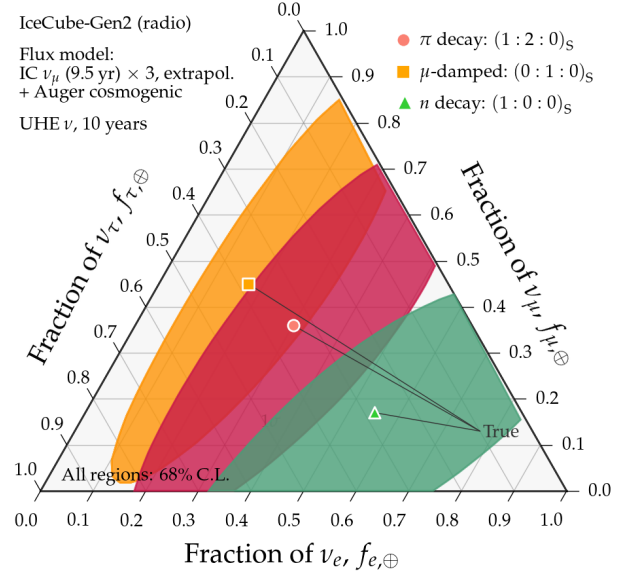
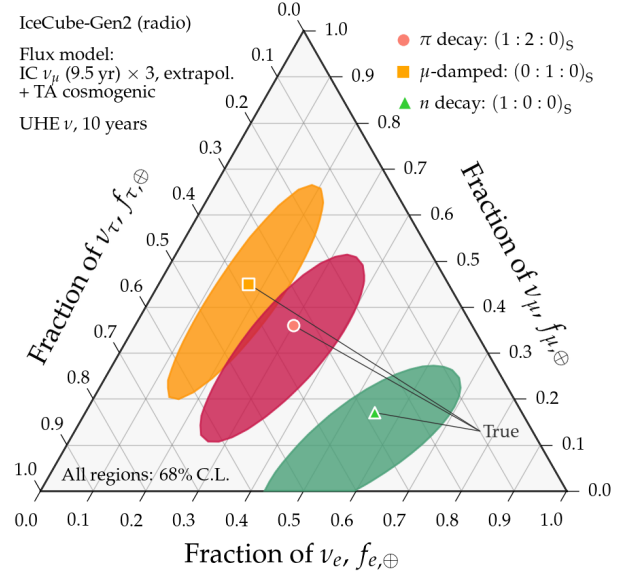


FIG. 12. *Measured flavor composition of the diffuse flux of UHE neutrinos in the radio array of IceCube-Gen2.* The regions represent the measurement uncertainty (68% C.L.) assuming as true each of our three benchmark cases of flavor composition in turn (Section IV B). *Top:* Results assuming our high all-flavor benchmark UHE neutrino flux, obtained from a fit to TA UHECR observations (Fig. 7). *Bottom:* Results assuming our low benchmark flux, obtained from a fit to Auger UHECR observations. See Fig. A1 in Appendix A for the full flavor likelihood and Section V for details. The in-ice radio-detection of UHE neutrinos may allow us, via our proposed methods (Section II), to measure their flavor composition, contingent on the size of their flux.

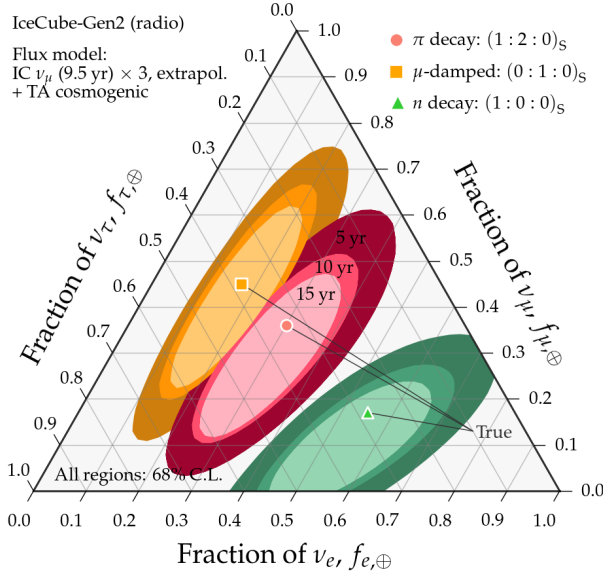


FIG. 13. *Measured flavor composition of the diffuse flux of UHE neutrinos in the radio array of IceCube-Gen2, varying detector exposure.* Similar to Fig. 12, which was generated assuming 10 years of detector exposure, but comparing results of assuming 5, 10, and 15 years of exposure. For this figure, we assume our high UHE neutrino benchmark flux. See Fig. 15 for associated results on the inferred flavor composition at the sources. *The increase in exposure from 10 to 15 years improves the precision with which flavor composition can be measured only marginally.*

CC interaction triggering a multi-shower event, i.e.,

$$p_{\mu,i}(\theta) = \frac{N_{\nu_{\mu},i}^{\text{CC}}(\theta)}{N_{\nu_{\text{all}},i}^{\text{CC}}(\theta)} r_{\mu,i}, \quad (9)$$

$$p_{\tau,i}(\theta) = \frac{N_{\nu_{\tau},i}^{\text{CC}}(\theta)}{N_{\nu_{\text{all}},i}^{\text{CC}}(\theta)} r_{\tau,i}, \quad (10)$$

and $r_{\mu,i}$ and $r_{\tau,i}$ are, respectively, the average fraction of ν_{μ} and ν_{τ} CC interactions that trigger multi-shower events (Fig. 3), averaged in energy inside the i -th bin. After profiling over the spectrum-shape parameters, the likelihood becomes $\mathcal{L}_{\text{mult}}(f_{e,\oplus}, f_{\mu,\oplus})$.

Figure 11 shows the resulting measurement of the flavor composition using multi-shower events alone. The measurement precision is comparable, but worse, than when using ν_e CC events alone. The measurement region is approximately aligned along the line $f_{\mu,\oplus} + f_{\tau,\oplus} = 2/3$, the expectation from the pion-decay benchmark. The offset from that is due to the fact that the multi-shower channel is also partially sensitive to the ν_e content. Due to the tilt of this region, the multi-shower detection channel is less effective, by itself, in distinguishing between our three benchmarks of flavor composition.

The fraction of multi-shower events (Fig. 3) depends on the station spacing—which we took to be 2 km—and on the station design, e.g., on using *deep* versus *shallow*

detector components, or a combination of them. While for the bare discovery of UHE neutrinos [90] isolating a large fraction of multi-shower events could be considered a needless reduction of the effective volume of the detector, the potential to constrain the flavor composition depends on such design considerations.

D. Total sensitivity

Finally, we combine all the available observables—the NC + CC events of all flavors, the events classified as ν_e CC, and the multi-shower events—to find the full flavor sensitivity of the radio array of IceCube-Gen2. Building on sections VB and VC, the likelihood function is

$$\mathcal{L}_{\text{ML+mult}}(\theta) = \prod_i^{N_E} \mathcal{P}(N_{\nu_{\text{all}},i}^{\text{obs}}; N_{\nu_{\text{all}},i}(\theta)) \times P_{\text{ML},i}(\theta) P_{\text{mult},i}(\theta), \quad (11)$$

where \mathcal{P} , $P_{\text{ML},i}$, and $P_{\text{mult},i}$ are defined as before. After profiling over the spectrum-shape parameters, this becomes $\mathcal{L}_{\text{ML+mult}}(f_{e,\oplus}, f_{\mu,\oplus})$.

Figure 12 shows our results, assuming our high and low benchmark fluxes and, separately, taking each of our three benchmark choices of flavor composition as the true one. As we pointed out in Section VB, the strong constraining power in the $f_{e,\oplus}$ direction is advantageous, since that is the dimension along which our benchmarks are the most separated. This reaffirms that, contingent on the neutrino flux being high enough, $f_{e,\oplus}$ could be measured with precision enough to distinguish between our three benchmark choices of flavor composition at 68% C.L. at the minimum—e.g., between full pion decay and muon-damped pion decay—to significantly more than 95% C.L.—e.g., between muon-damped pion decay and neutron decay.

The addition of multi-shower events grants us sensitivity to the non- ν_e content. In Fig. 12, it is what allows us to disfavor low and high content of ν_{μ} and ν_{τ} , and to close the 68% C.L. measurement contours, rather than being able only to measure bands of constant $f_{e,\oplus}$ or of approximately constant $f_{\mu,\oplus} + f_{\tau,\oplus}$, as in Fig. 11. While this does not significantly improve our capability to distinguish between our three flavor-composition benchmarks, it still reduces the measurement errors of the non- ν_e content. In addition, it allows us to probe predictions of the flavor composition with a low or high ν_{μ} or ν_{τ} content, as posited by numerous proposed models of new neutrino physics (Section VI).

When repeating the analysis using our low benchmark flux model, Fig. 12 shows that the measurement uncertainty deteriorates due to the approximate factor-of-three reduction in the number of detected events. The larger uncertainties render the distinction between alternative choices of flavor composition unfeasible, except for the ones most different from each other, like muon-damped and neutron decay. Unsurprisingly, like at lower energies,

the measurement of the UHE flavor composition hinges on the flux being sufficiently large. Still, Fig. 12 reveals that while a lower neutrino flux would practically remove any sensitivity to $f_{\mu,\oplus}$ and $f_{\tau,\oplus}$, it would only erode, but not destroy, the sensitivity to $f_{e,\oplus}$.

Figure 13 shows that increasing the detector exposure from 10 to 15 years only improves the precision of flavor measurements marginally. We show how the results change under our low benchmark flux, when increasing the exposure from 10 to 20 years in Fig. A2. Ultimately, improving the precision beyond what is shown in Fig. 13, within a reasonable time frame, would require improving the identification of ν_e CC events or exploiting additional flavor-sensitive channels or the combined detection by multiple UHE neutrino telescopes (Section II C); see, e.g., Fig. 1 in Ref. [132].

VI. APPLICATIONS

Below we provide a non-exhaustive list of salient applications made available by the measurement of the UHE neutrino flavor composition, several of which extend those available by flavor measurements at lower energies [6, 7, 31, 65, 66, 70].

Inferring the flavor composition at production:

Figure 14 shows the projected flavor composition of UHE neutrinos at their sources, $f_{\alpha,S}$, inferred from the flavor composition of UHE neutrinos measured at Earth, $f_{\alpha,\oplus}$, that we derived above, assuming our high benchmark flux. Inferring it allows us to probe the neutrino production mechanism, the physical conditions present in the sources, and ultimately their identity. We infer the flavor composition at the sources using the method introduced in Ref. [30] (see also Refs. [13, 132]), which inverts the effect of the flavor mixing that acts during neutrino propagation. In our projections in Fig. 14, we assume perfect knowledge of the values of the neutrino mixing parameters, which approximates the scenario expected for 2040, when the mixing angles should be known precisely enough to not add additional uncertainties [13] (Section IV B). Depending on the true flavor composition, $f_{e,S}$ could be inferred to within roughly 14–50% in 10 years. Assuming instead our low benchmark flux weakens the precision to roughly 30–80%; see Fig. A3.

Figure 15 shows that increasing the detector exposure from 10 to 15 years improves the precision on $f_{e,S}$ slightly, in agreement with the improvement on the measured $f_{\alpha,\oplus}$ shown in Fig. 13. Similarly to that case, exploiting the combined detection by multiple UHE neutrinos telescopes might improve the precision on $f_{e,S}$ further; see, e.g., Fig. 2 in Ref. [132].

Together, Figs. 14 and 15 (also Fig. A3) show that the precision with which we can infer the flavor

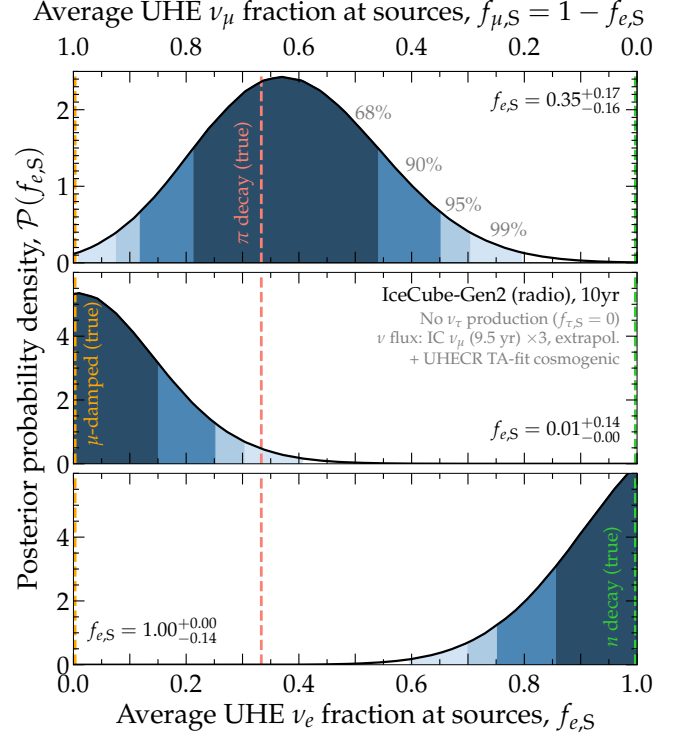


FIG. 14. *Projected posterior probability distribution of the inferred fraction of UHE ν_e at their sources.* The true flavor composition at the sources is assumed to be the benchmark from the full pion decay (top), muon-damped pion decay (center), and neutron decay (bottom). We assume perfect knowledge of the neutrino mixing parameters, given the expected upcoming improvement in their precision [13], and no production of ν_τ . For this figure, we assume our high benchmark UHE neutrino flux (Fig. 7), derived from fitting the UHECR spectrum and mass composition to observations from TA. See Fig. A3 for results assuming our low benchmark flux, Fig. 15 for varying detector exposure, and Section VI for details. *The in-ice radio-detection of UHE neutrinos may allow us to distinguish between alternative neutrino production mechanisms that yield different flavor composition.*

composition at the sources is better than what the underlying measurement of the flavor composition at Earth, in Figs. 12 and 13, might naively suggest. This is merely because when inferring the flavor composition at the sources we only measure a single flavor fraction, $f_{e,S}$, whereas when measuring the flavor composition at the Earth, we measure two, e.g., $f_{e,\oplus}$ and $f_{\mu,\oplus}$, since $f_{\tau,\oplus} \equiv 1 - f_{e,\oplus} - f_{\mu,\oplus}$, which dilutes the precision of the measurement.

Probing the magnetic field intensity inside UHE neutrino sources: Measuring a flavor composition compatible with neutrino production via muon-damped pion decay, $(0, 1, 0)_S$, would indirectly represent a measurement of the average intensity of the magnetic field inside UHE neutrino sources that is responsible for the synchrotron-

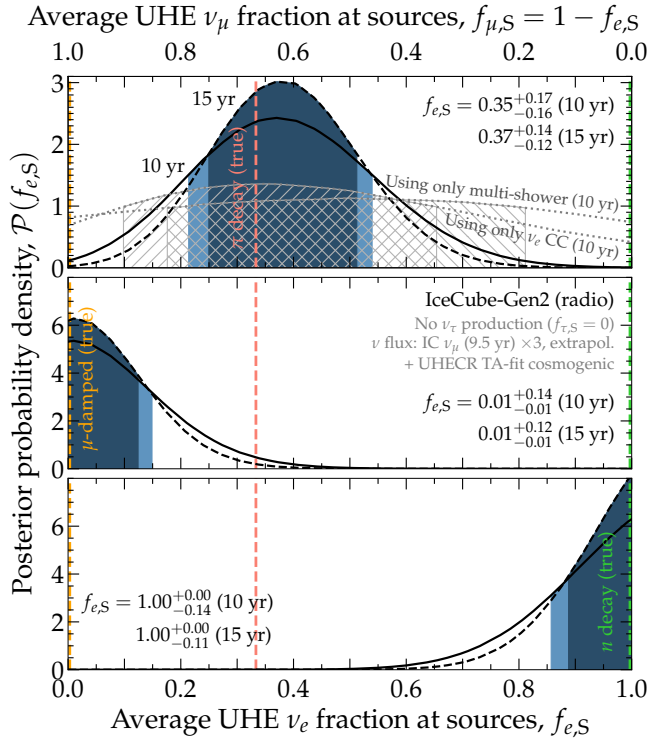


FIG. 15. *Projected posterior probability distribution of the inferred fraction of UHE ν_e at their sources, varying detector exposure.* Similar to Fig. 14, but comparing results obtained using 10 years (as in Fig. 14) and 15 years of detector exposure. Only for the benchmark flavor composition from the full pion decay (top), we show the result of using only one of our two flavor-sensitive channels (Sections II A and II B), as in Fig. 11. All intervals of $f_{e,S}$ are at 68% C.L. See Fig. 13 for associated measurements of the flavor composition at Earth and Section VI for details. *Even using a single flavor-sensitive channel could provide sensitivity to the UHE ν_e at the sources.*

cooling of intermediate muons (Section IV B). Conversely, measuring a different flavor composition can be used to set upper limits on the magnetic field intensity and, by proxy, to constrain the identity of the population of the neutrino sources. So far, this has been done using IceCube TeV–PeV neutrinos [27, 32]. However, they provide sensitivity to magnetic fields larger than about 10^4 G, which are believed to be harbored only by a few candidate source populations, like a subset of gamma-ray bursts. The synchrotron cooling of muons becomes important at energies roughly larger than $2 \cdot 10^9$ (Γ/B) GeV, where Γ is the bulk Lorentz factor of the neutrino production region and B is the magnetic field intensity [32]. Therefore, using UHE neutrinos would allow us to extend the sensitivity down to the 1 G scale, which would encompass significantly more candidate source populations that harbor weaker magnetic fields [32].

Distinguishing cosmogenic neutrinos from UHE source neutrinos: Cosmogenic neutrinos are made in extragalactic space via UHE proton-photon interactions on cosmological photon backgrounds (Section IV A). Because extragalactic magnetic fields are likely weak—nominally, of nG-scale—the flavor composition with which cosmogenic neutrinos are produced should be that of the full pion decay, i.e., $(\frac{1}{3}, \frac{2}{3}, 0)_S$. Therefore, were we to measure a flavor composition compatible with muon-damped pion decay, $(0, 1, 0)_S$, it would mean that the neutrinos were produced instead in the magnetized environment inside a cosmic accelerator. Given the variety in the shape of the energy spectrum of cosmogenic neutrinos and UHE source neutrinos, measuring the UHE neutrino flavor composition could provide the only feasible way to distinguish between the two should a diffuse UHE neutrino flux be discovered.

Probing neutrino physics at the highest energies:

Many proposed models of new physics that extend the Standard Model posit effects that grow with neutrino energy, including changes to the neutrino flavor composition. New physics may act at neutrino production, propagation, or detection [65, 66]. Examples include, at production, nonstandard neutrino production and nonstandard neutrino-matter interactions; during propagation, pseudo-Dirac neutrinos, neutrino decay, quantum decoherence, active-sterile neutrino mixing, effective operators, dark matter-neutrino interactions, new long-range neutrino-electron and neutrino-neutron interactions, and neutrino shortcuts through extra dimensions during propagation; and, at detection, nonstandard interactions inside the Earth and the detector. For a review, see Ref. [58].

Figure 1 maps the regions of flavor composition at Earth accessible with standard oscillations and with two general classes of new neutrino physics, as in Ref. [12], but forecast using the expected uncertainty on the mixing parameters in the year 2040. The first class resembles neutrino decay and changes the fractions of neutrino-mass eigenstates that reach Earth. The second class resembles Lorentz-invariance violation, which modified the neutrino propagation states by augmenting the neutrino Hamiltonian with a correction whose relative importance grows with neutrino energy. Figure 1 reveals that the UHE flavor sensitivity that we may achieve could potentially test extreme deviations in the flavor composition stemming from new physics, relative to the nominal expectation of approximate flavor equipartition.

VII. SUMMARY AND OUTLOOK

The discovery of UHE neutrinos, with energies above 10^{17} eV, might finally be within reach in the near future, thanks to a new generation of large-scale neutrino telescopes that are currently under planning. Upon discovering a diffuse flux of UHE neutrinos, measuring its flavor composition would grant us long-awaited insight into UHE neutrino physics and astrophysics to complement what can be gleaned from discovery and from measuring the neutrino energy spectrum. Yet, in spite of its latent potential, the measurement of the UHE neutrino flavor composition has received relatively little attention.

For the first time, in preparation for the upcoming opportunity, we have provided a method to measure the flavor composition of a diffuse UHE neutrino flux in upcoming in-ice radio-detection neutrino telescopes, such as RNO-G, presently under construction, and the radio array of IceCube-Gen2, in advanced stages of planning and to which we gear our results. We demonstrate the proof-of-principle, but realistic feasibility of our method via state-of-the-art modeling using the NuRadioMC code, including neutrino interactions and propagation of secondary leptons, the generation and in-ice propagation of the Askaryan radio emission they generate, and its detection by an array of underground antennas including a full detector and trigger simulation whose design matches the one envisioned for IceCube-Gen2.

The UHE flavor sensitivity stems from two separate, complementary observables that provide access to the ν_e content and to the $\nu_\mu + \nu_\tau$ content. On the one hand, the sensitivity to ν_e comes from the identification of charged-current interactions of ν_e . To identify them, we developed a dedicated neural network to identify the characteristic signature caused by the Landau-Pomeranchuk-Migdal effect. On the other hand, the sensitivity to $\nu_\mu + \nu_\tau$ comes from the identification of secondary interactions of muons and taus created in charged-current interactions of ν_μ and ν_τ . In a fraction of the events, Askaryan emission from the initial neutrino interaction and a secondary interaction of the lepton can be observed in separate detector stations.

Our results are promising. Yet, unavoidably, they depend on the size of the UHE neutrino flux, which is presently unknown. Assuming a high diffuse UHE neutrino benchmark flux that yields about 180 detected UHE neutrinos after 10 years of observation, we find not only that it would be possible for IceCube-Gen2 to measure the flavor composition, but to achieve enough precision to distinguish between three alternative benchmarks of

high-energy neutrino production that yield different flavor composition at Earth—pion decay, muon-damped pion decay, and neutron decay—at more than 68% C.L.

This sensitivity, combined with envisioned precise measurements of the neutrino mixing parameters, would allow us to further enhance our ability to distinguish between production mechanisms. Further, the measurements open up the possibility of testing extreme deviations in the flavor composition due to new neutrino physics acting at ultra-high energies. Using a factor-of-three lower neutrino flux weakens these prospects, but does not dispel them.

Discovering UHE neutrinos is bound to bring transformative progress to the field by answering long-held extant questions in high-energy physics and astrophysics. We have shown how to boost the insight we can glean from them by measuring their flavor composition in mature, upcoming in-ice radio-detection neutrino telescopes.

ACKNOWLEDGMENTS

CG and AC are supported by the Swedish Research Council (VETENSKAPSRÅDET) under project no. 2021-05449. MB is supported by VILLUM FONDEN under project no. 29388. This work used resources provided by the High-Performance Computing Center at the University of Copenhagen and resources provided by the National Academic Infrastructure for Supercomputing in Sweden (NAISS) and the Swedish National Infrastructure for Computing (SNIC) at UPPMAX partially funded by the Swedish Research Council through grant agreements no. 2022-06725 and no. 2018-05973.

Appendix A: Additional figures

Figure A1 shows the likelihood of flavor measurement, Eq. (11) in the main text, evaluated at all possible combinations of the flavor composition at Earth, $(f_e, f_\mu, f_\tau)_{\oplus}$.

Figure A2 shows the measured flavor composition at Earth, assuming our low UHE neutrino flux benchmark, and varying the detector exposure from 10 to 20 years. This should be compared to Fig. 13 in the main text.

Figure A3 shows the inferred content of UHE ν_e at the sources, assuming our low UHE neutrino flux benchmark. Compared to Fig. 14 in the main text, which is computed assuming our high UHE flux instead, the uncertainty in the measured value of $f_{e,\oplus}$ is about twice as large.

* alan.coleman@physics.uu.se

† christian.glaser@physics.uu.se

‡ mbustamante@nbi.ku.dk

[1] V. S. Berezinsky and G. T. Zatsepin, Cosmic rays at ultrahigh-energies (neutrino?), *Phys. Lett. B* **28**, 423

(1969).

[2] K. Greisen, End to the cosmic ray spectrum?, *Phys. Rev. Lett.* **16**, 748 (1966).

[3] G. T. Zatsepin and V. A. Kuzmin, Upper limit of the spectrum of cosmic rays, *JETP Lett.* **4**, 78 (1966).

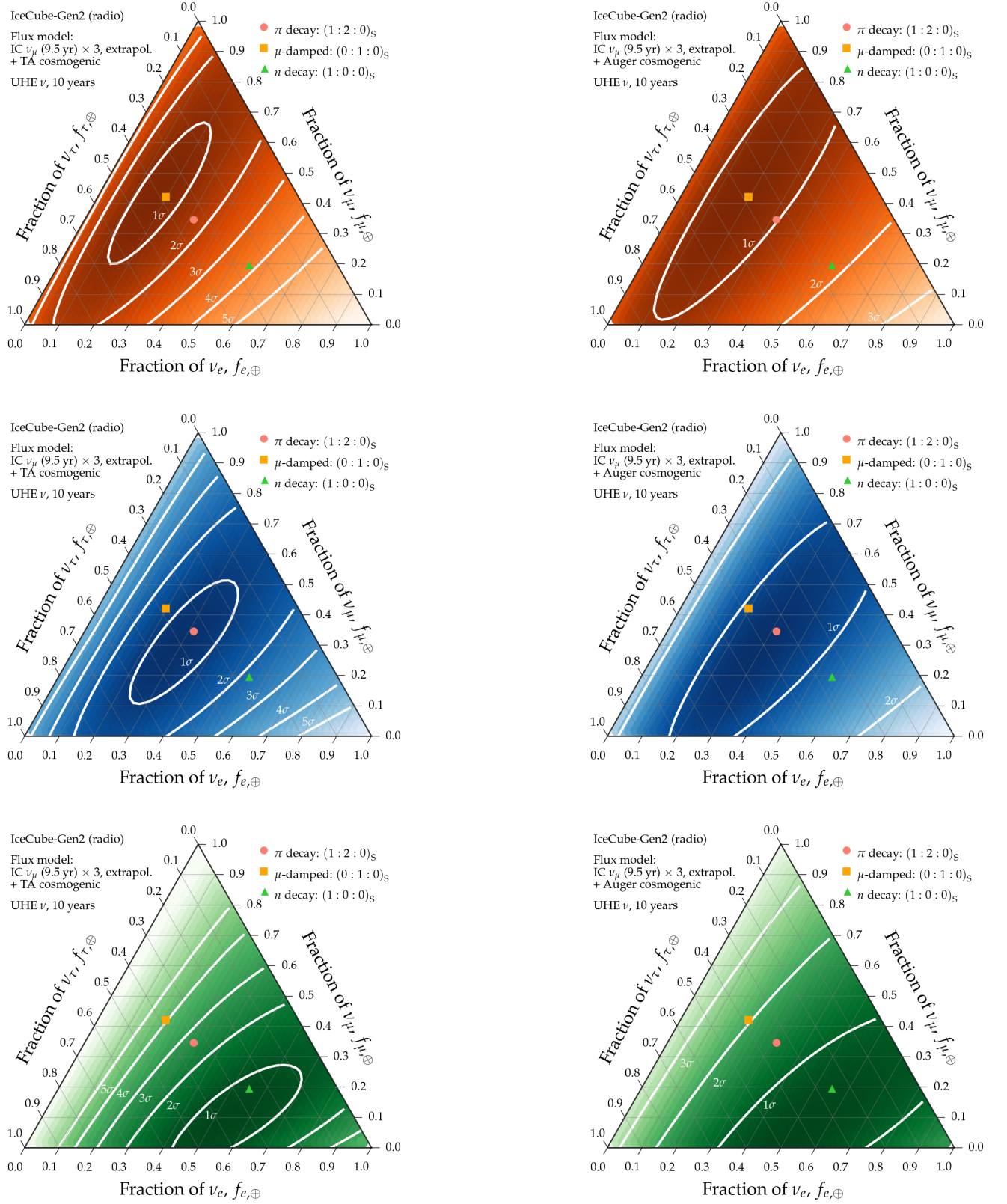


FIG. A1. *Likelihood of measuring the UHE neutrino flavor composition in the radio array of IceCube-Gen2, evaluated for all possible flavor compositions at Earth.* The UHE neutrino flux is assumed to be our high benchmark flux (left column) or low benchmark flux (right column); see Fig. 7 in the main text. The true flavor composition at the sources is assumed to be the benchmark from the full pion decay (top row), muon-damped pion decay (center row), and neutron decay (bottom row). The contours show allowed regions at difference confidence levels, calculated using Wilks' theorem; these are the contours shown in Figs. 1, 11, and 12.

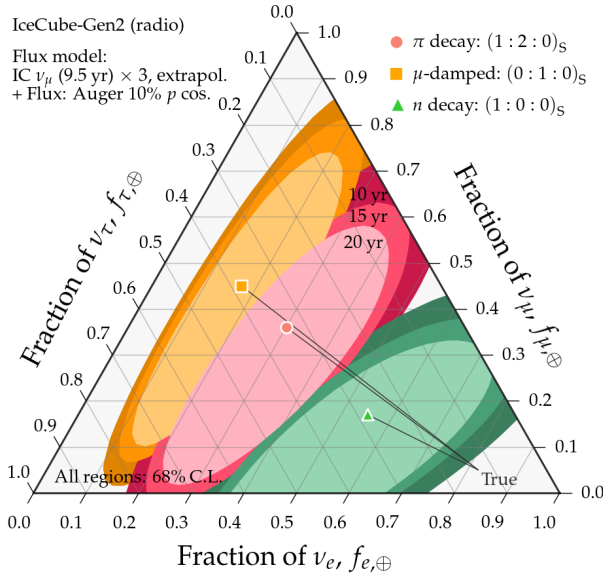


FIG. A2. *Measured flavor composition of the diffuse flux of UHE neutrinos in the radio array of IceCube-Gen2, varying detector exposure.* Similar to Fig. 13 in the main text, but assuming our low benchmark UHE neutrino flux (Fig. 7), derived from fitting the UHECR spectrum and mass composition to observations from Auger, with 10% of proton content. The contours correspond to 10, 15, and 20 years of data collection. See Fig. A3 for associated results on the inferred flavor composition at the sources.

- [4] M. G. Aartsen *et al.* (IceCube), Differential limit on the extremely-high-energy cosmic neutrino flux in the presence of astrophysical background from nine years of IceCube data, *Phys. Rev. D* **98**, 062003 (2018), [arXiv:1807.01820 \[astro-ph.HE\]](#).
- [5] A. Aab *et al.* (Pierre Auger), Probing the origin of ultra-high-energy cosmic rays with neutrinos in the EeV energy range using the Pierre Auger Observatory, *JCAP* **10**, 022, [arXiv:1906.07422 \[astro-ph.HE\]](#).
- [6] R. Mammen Abraham *et al.*, Tau neutrinos in the next decade: from GeV to EeV, *J. Phys. G* **49**, 110501 (2022), [arXiv:2203.05591 \[hep-ph\]](#).
- [7] M. Ackermann *et al.*, High-energy and ultra-high-energy neutrinos: A Snowmass white paper, *JHEAp* **36**, 55 (2022), [arXiv:2203.08096 \[hep-ph\]](#).
- [8] C. Guépin, K. Kotera, and F. Oikonomou, High-energy neutrino transients and the future of multi-messenger astronomy, *Nature Rev. Phys.* **4**, 697 (2022), [arXiv:2207.12205 \[astro-ph.HE\]](#).
- [9] S. Barwick and C. Glaser, Radio Detection of High Energy Neutrinos in Ice, published in *Neutrino Physics and Astrophysics*, edited by F. W. Stecker, in the *Encyclopedia of Cosmology II*, edited by G. G. Fazio, World Scientific Publishing Company, Singapore (2023), [arXiv:2208.04971 \[astro-ph.IM\]](#).
- [10] M. G. Aartsen *et al.* (IceCube-Gen2), IceCube-Gen2: the window to the extreme Universe, *J. Phys. G* **48**, 060501 (2021), [arXiv:2008.04323 \[astro-ph.HE\]](#).
- [11] R. Abbasi *et al.* (IceCube-Gen2), Sensitivity of

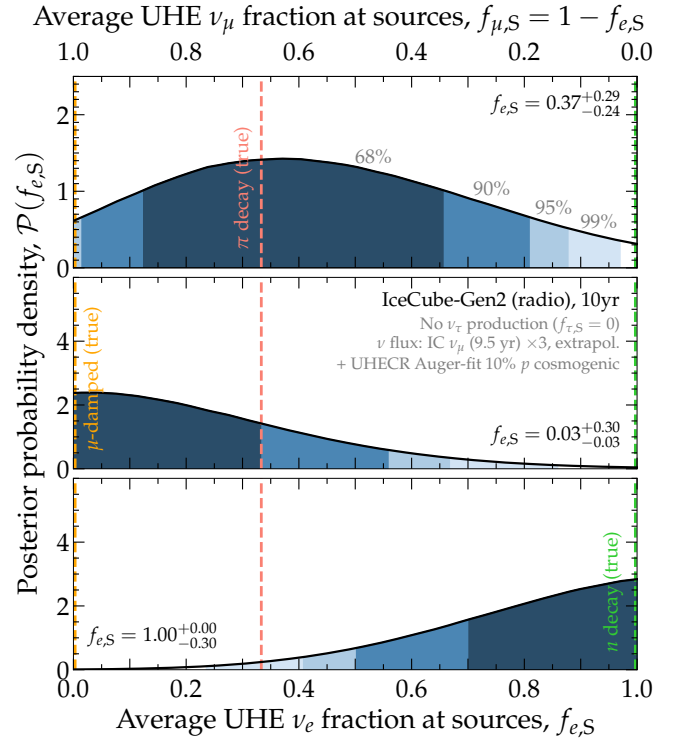


FIG. A3. *Projected posterior probability distribution of the inferred fraction of UHE ν_e at their sources.* Same as Fig. 14 in the main text, but assuming our benchmark UHE neutrino flux (Fig. 7), derived from fitting the UHECR spectrum and mass composition to observations from Auger, with 10% of proton content. See Section VI in the main text for details.

- IceCube-Gen2 to measure flavor composition of Astrophysical neutrinos, *PoS ICRC2023*, 1123 (2023), [arXiv:2308.15220 \[astro-ph.HE\]](#).
- [12] M. Bustamante, J. F. Beacom, and W. Winter, Theoretically palatable flavor combinations of astrophysical neutrinos, *Phys. Rev. Lett.* **115**, 161302 (2015), [arXiv:1506.02645 \[astro-ph.HE\]](#).
- [13] N. Song, S. W. Li, C. A. Argüelles, M. Bustamante, and A. C. Vincent, The Future of High-Energy Astrophysical Neutrino Flavor Measurements, *JCAP* **04**, 054, [arXiv:2012.12893 \[hep-ph\]](#).
- [14] J. P. Rachen and P. Mészáros, Photohadronic neutrinos from transients in astrophysical sources, *Phys. Rev. D* **58**, 123005 (1998), [arXiv:astro-ph/9802280](#).
- [15] H. Athar, M. Jezabek, and O. Yasuda, Effects of neutrino mixing on high-energy cosmic neutrino flux, *Phys. Rev. D* **62**, 103007 (2000), [arXiv:hep-ph/0005104](#).
- [16] R. M. Crocker, F. Melia, and R. R. Volkas, Searching for long wavelength neutrino oscillations in the distorted neutrino spectrum of galactic supernova remnants, *Astrophys. J. Suppl.* **141**, 147 (2002), [arXiv:astro-ph/0106090](#).
- [17] G. Barenboim and C. Quigg, Neutrino observatories can characterize cosmic sources and neutrino properties, *Phys. Rev. D* **67**, 073024 (2003), [arXiv:hep-ph/0301220](#).
- [18] J. F. Beacom, N. F. Bell, D. Hooper, S. Pakvasa, and T. J. Weiler, Measuring flavor ratios of high-energy as-

- trophysical neutrinos, *Phys. Rev. D* **68**, 093005 (2003), [Erratum: *Phys. Rev. D* **72**, 019901 (2005)], [arXiv:hep-ph/0307025](#).
- [19] J. F. Beacom and J. Candia, Shower power: Isolating the prompt atmospheric neutrino flux using electron neutrinos, *JCAP* **11**, 009, [arXiv:hep-ph/0409046](#).
- [20] T. Kashti and E. Waxman, Flavoring astrophysical neutrinos: Flavor ratios depend on energy, *Phys. Rev. Lett.* **95**, 181101 (2005), [arXiv:astro-ph/0507599](#).
- [21] O. Mena, I. Mocioiu, and S. Razzaque, Oscillation effects on high-energy neutrino fluxes from astrophysical hidden sources, *Phys. Rev. D* **75**, 063003 (2007), [arXiv:astro-ph/0612325](#).
- [22] M. Kachelrieß and R. Tomàs, High energy neutrino yields from astrophysical sources I: Weakly magnetized sources, *Phys. Rev. D* **74**, 063009 (2006), [arXiv:astro-ph/0606406](#).
- [23] P. Lipari, M. Lusignoli, and D. Meloni, Flavor Composition and Energy Spectrum of Astrophysical Neutrinos, *Phys. Rev. D* **75**, 123005 (2007), [arXiv:0704.0718 \[astro-ph\]](#).
- [24] A. Esmaili and Y. Farzan, An Analysis of Cosmic Neutrinos: Flavor Composition at Source and Neutrino Mixing Parameters, *Nucl. Phys. B* **821**, 197 (2009), [arXiv:0905.0259 \[hep-ph\]](#).
- [25] S. Choubey and W. Rodejohann, Flavor Composition of UHE Neutrinos at Source and at Neutrino Telescopes, *Phys. Rev. D* **80**, 113006 (2009), [arXiv:0909.1219 \[hep-ph\]](#).
- [26] S. Hümmer, M. Maltoni, W. Winter, and C. Yaguna, Energy dependent neutrino flavor ratios from cosmic accelerators on the Hillas plot, *Astropart. Phys.* **34**, 205 (2010), [arXiv:1007.0006 \[astro-ph.HE\]](#).
- [27] W. Winter, Photohadronic Origin of the TeV-PeV Neutrinos Observed in IceCube, *Phys. Rev. D* **88**, 083007 (2013), [arXiv:1307.2793 \[astro-ph.HE\]](#).
- [28] A. Palladino, G. Pagliaroli, F. L. Villante, and F. Vissani, What is the Flavor of the Cosmic Neutrinos Seen by IceCube?, *Phys. Rev. Lett.* **114**, 171101 (2015), [arXiv:1502.02923 \[astro-ph.HE\]](#).
- [29] D. Biehl, A. Fedynitch, A. Palladino, T. J. Weiler, and W. Winter, Astrophysical Neutrino Production Diagnostics with the Glashow Resonance, *JCAP* **01**, 033, [arXiv:1611.07983 \[astro-ph.HE\]](#).
- [30] M. Bustamante and M. Ahlers, Inferring the flavor of high-energy astrophysical neutrinos at their sources, *Phys. Rev. Lett.* **122**, 241101 (2019), [arXiv:1901.10087 \[astro-ph.HE\]](#).
- [31] M. Ackermann *et al.*, Astrophysics Uniquely Enabled by Observations of High-Energy Cosmic Neutrinos, *Bull. Am. Astron. Soc.* **51**, 185 (2019), [arXiv:1903.04334 \[astro-ph.HE\]](#).
- [32] M. Bustamante and I. Tamborra, Using high-energy neutrinos as cosmic magnetometers, *Phys. Rev. D* **102**, 123008 (2020), [arXiv:2009.01306 \[astro-ph.HE\]](#).
- [33] A. Bhattacharya, R. Enberg, M. H. Reno, and I. Sarcevic, Energy-dependent flavour ratios in neutrino telescopes from charm, (2023), [arXiv:2309.09139 \[astro-ph.HE\]](#).
- [34] B. Telalovic and M. Bustamante, Flavor Anisotropy in the High-Energy Astrophysical Neutrino Sky, (2023), [arXiv:2310.15224 \[astro-ph.HE\]](#).
- [35] P. S. B. Dev, S. Jana, and Y. Porto, Flavor Matters, but Matter Flavors: Matter Effects on Flavor Composition of Astrophysical Neutrinos, (2023), [arXiv:2312.17315 \[hep-ph\]](#).
- [36] J. F. Beacom, N. F. Bell, D. Hooper, S. Pakvasa, and T. J. Weiler, Decay of High-Energy Astrophysical Neutrinos, *Phys. Rev. Lett.* **90**, 181301 (2003), [arXiv:hep-ph/0211305](#).
- [37] J. F. Beacom, N. F. Bell, D. Hooper, J. G. Learned, S. Pakvasa, and T. J. Weiler, PseudoDirac neutrinos: A Challenge for neutrino telescopes, *Phys. Rev. Lett.* **92**, 011101 (2004), [arXiv:hep-ph/0307151](#).
- [38] J. F. Beacom, N. F. Bell, D. Hooper, S. Pakvasa, and T. J. Weiler, Sensitivity to θ_{13} and δ in the decaying astrophysical neutrino scenario, *Phys. Rev. D* **69**, 017303 (2004), [arXiv:hep-ph/0309267](#).
- [39] P. D. Serpico, Probing the 2-3 leptonic mixing at high-energy neutrino telescopes, *Phys. Rev. D* **73**, 047301 (2006), [arXiv:hep-ph/0511313](#).
- [40] S. Pakvasa, W. Rodejohann, and T. J. Weiler, Flavor Ratios of Astrophysical Neutrinos: Implications for Precision Measurements, *JHEP* **02**, 005, [arXiv:0711.4517 \[hep-ph\]](#).
- [41] A. Esmaili, Pseudo-Dirac Neutrino Scenario: Cosmic Neutrinos at Neutrino Telescopes, *Phys. Rev. D* **81**, 013006 (2010), [arXiv:0909.5410 \[hep-ph\]](#).
- [42] A. Bhattacharya, S. Choubey, R. Gandhi, and A. Watanabe, Diffuse Ultra-High Energy Neutrino Fluxes and Physics Beyond the Standard Model, *Phys. Lett. B* **690**, 42 (2010), [arXiv:0910.4396 \[hep-ph\]](#).
- [43] A. Bhattacharya, S. Choubey, R. Gandhi, and A. Watanabe, Ultra-high neutrino fluxes as a probe for non-standard physics, *JCAP* **09**, 009, [arXiv:1006.3082 \[hep-ph\]](#).
- [44] M. Bustamante, A. M. Gago, and C. Peña-Garay, Energy-Independent New Physics in the Flavour Ratios of High-Energy Astrophysical Neutrinos, *JHEP* **04**, 066, [arXiv:1001.4878 \[hep-ph\]](#).
- [45] P. Mehta and W. Winter, Interplay of energy dependent astrophysical neutrino flavor ratios and new physics effects, *JCAP* **03**, 041, [arXiv:1101.2673 \[hep-ph\]](#).
- [46] P. Baerwald, M. Bustamante, and W. Winter, Neutrino Decays over Cosmological Distances and the Implications for Neutrino Telescopes, *JCAP* **10**, 020, [arXiv:1208.4600 \[astro-ph.CO\]](#).
- [47] L. Fu, C. M. Ho, and T. J. Weiler, Cosmic Neutrino Flavor Ratios with Broken $\nu_\mu - \nu_\tau$ Symmetry, *Phys. Lett. B* **718**, 558 (2012), [arXiv:1209.5382 \[hep-ph\]](#).
- [48] S. Pakvasa, A. Joshipura, and S. Mohanty, Explanation for the low flux of high energy astrophysical muon-neutrinos, *Phys. Rev. Lett.* **110**, 171802 (2013), [arXiv:1209.5630 \[hep-ph\]](#).
- [49] A. Chatterjee, M. M. Devi, M. Ghosh, R. Moharana, and S. K. Raut, Probing CP violation with the first three years of ultrahigh energy neutrinos from IceCube, *Phys. Rev. D* **90**, 073003 (2014), [arXiv:1312.6593 \[hep-ph\]](#).
- [50] X.-J. Xu, H.-J. He, and W. Rodejohann, Constraining Astrophysical Neutrino Flavor Composition from Leptonic Unitarity, *JCAP* **12**, 039, [arXiv:1407.3736 \[hep-ph\]](#).
- [51] E. Aeikens, H. Päs, S. Pakvasa, and P. Sicking, Flavor ratios of extragalactic neutrinos and neutrino shortcuts in extra dimensions, *JCAP* **10**, 005, [arXiv:1410.0408 \[hep-ph\]](#).
- [52] C. A. Argüelles, T. Katori, and J. Salvadó, New Physics

- in Astrophysical Neutrino Flavor, *Phys. Rev. Lett.* **115**, 161303 (2015), [arXiv:1506.02043 \[hep-ph\]](#).
- [53] G. Pagliaroli, A. Palladino, F. L. Villante, and F. Visani, Testing nonradiative neutrino decay scenarios with IceCube data, *Phys. Rev. D* **92**, 113008 (2015), [arXiv:1506.02624 \[hep-ph\]](#).
- [54] I. M. Shoemaker and K. Murase, Probing BSM Neutrino Physics with Flavor and Spectral Distortions: Prospects for Future High-Energy Neutrino Telescopes, *Phys. Rev. D* **93**, 085004 (2016), [arXiv:1512.07228 \[astro-ph.HE\]](#).
- [55] P. F. de Salas, R. A. Lineros, and M. Tórtola, Neutrino propagation in the galactic dark matter halo, *Phys. Rev. D* **94**, 123001 (2016), [arXiv:1601.05798 \[astro-ph.HE\]](#).
- [56] M. C. Gonzalez-García, M. Maltoni, I. Martínez-Soler, and N. Song, Non-standard neutrino interactions in the Earth and the flavor of astrophysical neutrinos, *Astropart. Phys.* **84**, 15 (2016), [arXiv:1605.08055 \[hep-ph\]](#).
- [57] M. Bustamante, J. F. Beacom, and K. Murase, Testing decay of astrophysical neutrinos with incomplete information, *Phys. Rev. D* **95**, 063013 (2017), [arXiv:1610.02096 \[astro-ph.HE\]](#).
- [58] R. W. Rasmussen, L. Lechner, M. Ackermann, M. Kowalski, and W. Winter, Astrophysical neutrinos flavored with Beyond the Standard Model physics, *Phys. Rev. D* **96**, 083018 (2017), [arXiv:1707.07684 \[hep-ph\]](#).
- [59] U. K. Dey, D. Kar, M. Mitra, M. Spannowsky, and A. C. Vincent, Searching for Leptoquarks at IceCube and the LHC, *Phys. Rev. D* **98**, 035014 (2018), [arXiv:1709.02009 \[hep-ph\]](#).
- [60] M. Bustamante and S. K. Agarwalla, Universe's Worth of Electrons to Probe Long-Range Interactions of High-Energy Astrophysical Neutrinos, *Phys. Rev. Lett.* **122**, 061103 (2019), [arXiv:1808.02042 \[astro-ph.HE\]](#).
- [61] Y. Farzan and S. Palomares-Ruiz, Flavor of cosmic neutrinos preserved by ultralight dark matter, *Phys. Rev. D* **99**, 051702 (2019), [arXiv:1810.00892 \[hep-ph\]](#).
- [62] M. Ahlers, M. Bustamante, and S. Mu, Unitarity Bounds of Astrophysical Neutrinos, *Phys. Rev. D* **98**, 123023 (2018), [arXiv:1810.00893 \[astro-ph.HE\]](#).
- [63] V. Brdar and R. S. L. Hansen, IceCube Flavor Ratios with Identified Astrophysical Sources: Towards Improving New Physics Testability, *JCAP* **02**, 023, [arXiv:1812.05541 \[hep-ph\]](#).
- [64] A. Palladino, The flavor composition of astrophysical neutrinos after 8 years of IceCube: an indication of neutron decay scenario?, *Eur. Phys. J. C* **79**, 500 (2019), [arXiv:1902.08630 \[astro-ph.HE\]](#).
- [65] M. Ackermann *et al.*, Fundamental Physics with High-Energy Cosmic Neutrinos, *Bull. Am. Astron. Soc.* **51**, 215 (2019), [arXiv:1903.04333 \[astro-ph.HE\]](#).
- [66] C. A. Argüelles, M. Bustamante, A. Kheirandish, S. Palomares-Ruiz, J. Salvado, and A. C. Vincent, Fundamental physics with high-energy cosmic neutrinos today and in the future, *PoS ICRC2019*, 849 (2020), [arXiv:1907.08690 \[astro-ph.HE\]](#).
- [67] M. Ahlers, M. Bustamante, and N. G. N. Willesen, Flavors of astrophysical neutrinos with active-sterile mixing, *JCAP* **07**, 029, [arXiv:2009.01253 \[hep-ph\]](#).
- [68] S. Karmakar, S. Pandey, and S. Rakshit, Astronomy with energy dependent flavour ratios of extragalactic neutrinos, *JHEP* **10**, 004, [arXiv:2010.07336 \[hep-ph\]](#).
- [69] D. F. G. Fiorillo, G. Mangano, S. Morisi, and O. Pisanti, IceCube constraints on violation of equivalence principle, *JCAP* **04**, 079, [arXiv:2012.07867 \[hep-ph\]](#).
- [70] C. A. Argüelles *et al.*, Snowmass white paper: beyond the standard model effects on neutrino flavor: Submitted to the proceedings of the US community study on the future of particle physics (Snowmass 2021), *Eur. Phys. J. C* **83**, 15 (2023), [arXiv:2203.10811 \[hep-ph\]](#).
- [71] O. Mena, S. Palomares-Ruiz, and A. C. Vincent, Flavor Composition of the High-Energy Neutrino Events in IceCube, *Phys. Rev. Lett.* **113**, 091103 (2014), [arXiv:1404.0017 \[astro-ph.HE\]](#).
- [72] S. Palomares-Ruiz, A. C. Vincent, and O. Mena, Spectral analysis of the high-energy IceCube neutrinos, *Phys. Rev. D* **91**, 103008 (2015), [arXiv:1502.02649 \[astro-ph.HE\]](#).
- [73] M. G. Aartsen *et al.* (IceCube), Flavor Ratio of Astrophysical Neutrinos above 35 TeV in IceCube, *Phys. Rev. Lett.* **114**, 171102 (2015), [arXiv:1502.03376 \[astro-ph.HE\]](#).
- [74] A. Palladino and F. Vissani, The natural parameterization of cosmic neutrino oscillations, *Eur. Phys. J. C* **75**, 433 (2015), [arXiv:1504.05238 \[hep-ph\]](#).
- [75] M. G. Aartsen *et al.* (IceCube), A combined maximum-likelihood analysis of the high-energy astrophysical neutrino flux measured with IceCube, *Astrophys. J.* **809**, 98 (2015), [arXiv:1507.03991 \[astro-ph.HE\]](#).
- [76] A. C. Vincent, S. Palomares-Ruiz, and O. Mena, Analysis of the 4-year IceCube high-energy starting events, *Phys. Rev. D* **94**, 023009 (2016), [arXiv:1605.01556 \[astro-ph.HE\]](#).
- [77] R. Abbasi *et al.* (IceCube), Detection of astrophysical tau neutrino candidates in IceCube, *Eur. Phys. J. C* **82**, 1031 (2022), [arXiv:2011.03561 \[hep-ex\]](#).
- [78] G. A. Askar'yan, Excess negative charge of an electron-photon shower and its coherent radio emission, *Zh. Eksp. Teor. Fiz.* **41**, 616 (1961).
- [79] I. Kravchenko *et al.* (RICE), Performance and simulation of the RICE detector, *Astropart. Phys.* **19**, 15 (2003), [arXiv:astro-ph/0112372](#).
- [80] A. Anker *et al.*, A search for cosmogenic neutrinos with the ARIANNA test bed using 4.5 years of data, *JCAP* **03**, 053, [arXiv:1909.00840 \[astro-ph.IM\]](#).
- [81] P. Allison *et al.* (ARA), Constraints on the diffuse flux of ultrahigh energy neutrinos from four years of Askaryan Radio Array data in two stations, *Phys. Rev. D* **102**, 043021 (2020), [arXiv:1912.00987 \[astro-ph.HE\]](#).
- [82] A. Anker *et al.* (ARIANNA), Probing the angular and polarization reconstruction of the ARIANNA detector at the South Pole, *JINST* **15** (09), P09039, [arXiv:2006.03027 \[astro-ph.IM\]](#).
- [83] A. Anker *et al.* (ARIANNA), Measuring the polarization reconstruction resolution of the ARIANNA neutrino detector with cosmic rays, *JCAP* **04** (04), 022, [arXiv:2112.01501 \[astro-ph.HE\]](#).
- [84] P. Allison *et al.* (ARA), Low-threshold ultrahigh-energy neutrino search with the Askaryan Radio Array, *Phys. Rev. D* **105**, 122006 (2022), [arXiv:2202.07080 \[astro-ph.HE\]](#).
- [85] J. A. Aguilar *et al.* (RNO-G), Design and Sensitivity of the Radio Neutrino Observatory in Greenland (RNO-G), *JINST* **16** (03), P03025, [Erratum: *JINST* **18**, E03001 (2023)], [arXiv:2010.12279 \[astro-ph.IM\]](#).
- [86] S. Hallmann, B. Clark, C. Glaser, D. Smith, *et al.* (IceCube-Gen2), Sensitivity studies for the IceCube-Gen2 radio array, *PoS ICRC2021*, 1183 (2021), [arXiv:2107.08910 \[astro-ph.HE\]](#).

- [87] IceCube-Gen2 Technical Design Report, <https://icecube-gen2.wisc.edu/science/publications/TDR>.
- [88] V. B. Valera, M. Bustamante, and C. Glaser, The ultra-high-energy neutrino-nucleon cross section: measurement forecasts for an era of cosmic EeV-neutrino discovery, *JHEP* **06**, 105, [arXiv:2204.04237 \[hep-ph\]](#).
- [89] D. F. G. Fiorillo, M. Bustamante, and V. B. Valera, Near-future discovery of point sources of ultra-high-energy neutrinos, *JCAP* **03**, 026, [arXiv:2205.15985 \[astro-ph.HE\]](#).
- [90] V. B. Valera, M. Bustamante, and C. Glaser, Near-future discovery of the diffuse flux of ultrahigh-energy cosmic neutrinos, *Phys. Rev. D* **107**, 043019 (2023), [arXiv:2210.03756 \[astro-ph.HE\]](#).
- [91] V. B. Valera, M. Bustamante, and O. Mena, Joint measurement of the ultra-high-energy neutrino spectrum and cross section, (2023), [arXiv:2308.07709 \[astro-ph.HE\]](#).
- [92] L. A. Anchordoqui, Ultra-High-Energy Cosmic Rays, *Phys. Rept.* **801**, 1 (2019), [arXiv:1807.09645 \[astro-ph.HE\]](#).
- [93] R. Alves Batista *et al.*, Open Questions in Cosmic-Ray Research at Ultrahigh Energies, *Front. Astron. Space Sci.* **6**, 23 (2019), [arXiv:1903.06714 \[astro-ph.HE\]](#).
- [94] I. Esteban, S. Prohira, and J. F. Beacom, Detector requirements for model-independent measurements of ultrahigh energy neutrino cross sections, *Phys. Rev. D* **106**, 023021 (2022), [arXiv:2205.09763 \[hep-ph\]](#).
- [95] C. Glaser *et al.*, NuRadioMC: Simulating the radio emission of neutrinos from interaction to detector, *Eur. Phys. J. C* **80**, 77 (2020), [arXiv:1906.01670 \[astro-ph.IM\]](#).
- [96] D. García-Fernández, A. Nelles, and C. Glaser, Signatures of secondary leptons in radio-neutrino detectors in ice, *Phys. Rev. D* **102**, 083011 (2020), [arXiv:2003.13442 \[astro-ph.HE\]](#).
- [97] C. Glaser, D. García-Fernández, and A. Nelles, Prospects for neutrino-flavor physics with in-ice radio detectors, *PoS ICRC2021*, 1231 (2021).
- [98] O. Ericsson, *Investigations into neutrino flavor reconstruction from radio detector data using convolutional neural networks*, Bachelor's thesis, Uppsala University (2021).
- [99] S. Stjärnholm, O. Ericsson, and C. Glaser, Neutrino direction and flavor reconstruction from radio detector data using deep convolutional neural networks, *PoS ICRC2021*, 1055 (2021).
- [100] R. Brock *et al.* (CTEQ), Handbook of perturbative QCD: Version 1.0, *Rev. Mod. Phys.* **67**, 157 (1995).
- [101] J. M. Conrad, M. H. Shaevitz, and T. Bolton, Precision measurements with high-energy neutrino beams, *Rev. Mod. Phys.* **70**, 1341 (1998), [arXiv:hep-ex/9707015](#).
- [102] J. A. Formaggio and G. P. Zeller, From eV to EeV: Neutrino Cross Sections Across Energy Scales, *Rev. Mod. Phys.* **84**, 1307 (2012), [arXiv:1305.7513 \[hep-ex\]](#).
- [103] M. G. Aartsen *et al.* (IceCube), Measurement of the multi-TeV neutrino cross section with IceCube using Earth absorption, *Nature* **551**, 596 (2017), [arXiv:1711.08119 \[hep-ex\]](#).
- [104] M. Bustamante and A. Connolly, Extracting the Energy-Dependent Neutrino-Nucleon Cross Section above 10 TeV Using IceCube Showers, *Phys. Rev. Lett.* **122**, 041101 (2019), [arXiv:1711.11043 \[astro-ph.HE\]](#).
- [105] M. G. Aartsen *et al.* (IceCube), Measurements using the inelasticity distribution of multi-TeV neutrino interactions in IceCube, *Phys. Rev. D* **99**, 032004 (2019), [arXiv:1808.07629 \[hep-ex\]](#).
- [106] R. Abbasi *et al.* (IceCube), Measurement of the high-energy all-flavor neutrino-nucleon cross section with IceCube, *Phys. Rev. D* **104**, 022001 (2021), [arXiv:2011.03560 \[hep-ex\]](#).
- [107] A. Bishop *et al.* (ARA), Benefits of Looking for Coincident Events, Taus, and Muons with the Askaryan Radio Array, *PoS ICRC2023*, 1169 (2023), [arXiv:2308.07401 \[astro-ph.HE\]](#).
- [108] C. Glaser, A. Nelles, I. Plaisier, C. Welling, S. W. Barwick, D. García-Fernández, G. Gaswint, R. Lahmann, and C. Persichilli, NuRadioReco: A reconstruction framework for radio neutrino detectors, *Eur. Phys. J. C* **79**, 464 (2019), [arXiv:1903.07023 \[astro-ph.IM\]](#).
- [109] S. Barwick *et al.* (ARIANNA), Capabilities of ARIANNA: Neutrino Pointing Resolution and Implications for Future Ultra-high Energy Neutrino Astronomy, *PoS ICRC2021*, 1151 (2021).
- [110] J. A. Aguilar *et al.*, Reconstructing the neutrino energy for in-ice radio detectors: A study for the Radio Neutrino Observatory Greenland (RNO-G), *Eur. Phys. J. C* **82**, 147 (2022), [arXiv:2107.02604 \[astro-ph.HE\]](#).
- [111] C. Glaser, S. McAleer, S. Stjärnholm, P. Baldi, and S. W. Barwick, Deep-learning-based reconstruction of the neutrino direction and energy for in-ice radio detectors, *Astropart. Phys.* **145**, 102781 (2023), [arXiv:2205.15872 \[astro-ph.IM\]](#).
- [112] I. Plaisier, S. Bouma, and A. Nelles, Reconstructing the arrival direction of neutrinos in deep in-ice radio detectors, *Eur. Phys. J. C* **83**, 443 (2023), [arXiv:2302.00054 \[astro-ph.HE\]](#).
- [113] S. Bouma *et al.* (IceCube-Gen2), Direction reconstruction performance for IceCube-Gen2 Radio, *PoS ICRC2023*, 1045 (2023).
- [114] N. Heyer *et al.* (IceCube-Gen2), Deep Learning Based Event Reconstruction for the IceCube-Gen2 Radio Detector, *PoS ICRC2023*, 1102 (2023), [arXiv:2308.00164 \[astro-ph.HE\]](#).
- [115] L. Pyras, C. Glaser, S. Hallmann, and A. Nelles, Atmospheric muons at PeV energies in radio neutrino detectors, *JCAP* **10**, 043, [arXiv:2307.04736 \[astro-ph.HE\]](#).
- [116] L. D. Landau and I. Pomeranchuk, Limits of applicability of the theory of bremsstrahlung electrons and pair production at high-energies, *Dokl. Akad. Nauk Ser. Fiz.* **92**, 535 (1953).
- [117] L. D. Landau and I. Pomeranchuk, Electron-Cascade Processes at Ultra-High Energies, *Dokl. Akad. Nauk SSSR* **92**, 10.1016/b978-0-08-010586-4.50081-x (1965).
- [118] A. B. Migdal, Bremsstrahlung and pair production in condensed media at high-energies, *Phys. Rev.* **103**, 1811 (1956).
- [119] L. Gerhardt and S. R. Klein, Electron and Photon Interactions in the Regime of Strong LPM Suppression, *Phys. Rev. D* **82**, 074017 (2010), [arXiv:1007.0039 \[hep-ph\]](#).
- [120] S. R. Klein, S. A. Robertson, and R. Vogt, Nuclear effects in high-energy neutrino interactions, *Phys. Rev. C* **102**, 015808 (2020), [arXiv:2001.03677 \[hep-ph\]](#).
- [121] J. Álvarez-Muñiz, A. Romero-Wolf, and E. Zas, Practical and accurate calculations of Askaryan radiation,

- Phys. Rev. D **84**, 103003 (2011), [arXiv:1106.6283 \[astro-ph.HE\]](#).
- [122] R. L. Workman *et al.* (Particle Data Group), Review of Particle Physics, *PTEP* **2022**, 083C01 (2022).
 - [123] S. Ritz and D. Seckel, Detailed Neutrino Spectra From Cold Dark Matter Annihilations in the Sun, *Nucl. Phys. B* **304**, 877 (1988).
 - [124] F. Halzen and D. Saltzberg, Tau-neutrino appearance with a 1000 Megaparsec baseline, *Phys. Rev. Lett.* **81**, 4305 (1998), [arXiv:hep-ph/9804354](#).
 - [125] I. Safa, A. Pizzuto, C. A. Argüelles, F. Halzen, R. Hussain, A. Kheirandish, and J. Vandenbroucke, Observing EeV neutrinos through Earth: GZK and the anomalous ANITA events, *JCAP* **01**, 012, [arXiv:1909.10487 \[hep-ph\]](#).
 - [126] A. García, R. Gauld, A. Heijboer, and J. Rojo, Complete predictions for high-energy neutrino propagation in matter, *JCAP* **09**, 025, [arXiv:2004.04756 \[hep-ph\]](#).
 - [127] I. Safa, J. Lazar, A. Pizzuto, O. Vasquez, C. A. Argüelles, and J. Vandenbroucke, TauRunner: A public Python program to propagate neutral and charged leptons, *Comput. Phys. Commun.* **278**, 108422 (2022), [arXiv:2110.14662 \[hep-ph\]](#).
 - [128] V. B. Valera and M. Bustamante, (2023), private communication.
 - [129] R. Abbasi *et al.* (IceCube), IceCube Search for Earth-traversing ultra-high energy Neutrinos, *PoS ICRC2021*, 1170 (2021).
 - [130] S.-H. Wang, P. Chen, M. Huang, and J. Nam, Feasibility of Determining Diffuse Ultra-High Energy Cosmic Neutrino Flavor Ratio through ARA Neutrino Observatory, *JCAP* **11**, 062, [arXiv:1302.1586 \[astro-ph.HE\]](#).
 - [131] J. H. Koehne, K. Frantzen, M. Schmitz, T. Fuchs, W. Rhode, D. Chirkin, and J. Becker Tjus, PROPOSAL: A tool for propagation of charged leptons, *Comput. Phys. Commun.* **184**, 2070 (2013).
 - [132] F. Testagrossa, D. F. G. Fiorillo, and M. Bustamante, Two-detector flavor sensitivity to ultra-high-energy cosmic neutrinos, (2023), [arXiv:2310.12215 \[astro-ph.HE\]](#).
 - [133] D. Bergman (Telescope Array), Telescope Array Combined Fit to Cosmic Ray Spectrum and Composition, *PoS ICRC2021*, 338 (2021).
 - [134] A. van Vliet, R. Alves Batista, and J. R. Hörandel, Determining the fraction of cosmic-ray protons at ultra-high energies with cosmogenic neutrinos, *Phys. Rev. D* **100**, 021302 (2019), [arXiv:1901.01899 \[astro-ph.HE\]](#).
 - [135] R. Abbasi *et al.* (IceCube), Improved Characterization of the Astrophysical Muon-neutrino Flux with 9.5 Years of IceCube Data, *Astrophys. J.* **928**, 50 (2022), [arXiv:2111.10299 \[astro-ph.HE\]](#).
 - [136] K. Simonyan and A. Zisserman, Very Deep Convolutional Networks for Large-Scale Image Recognition, (2014), [arXiv:1409.1556 \[cs.CV\]](#).
 - [137] A. Anker *et al.* (ARIANNA), Improving sensitivity of the ARIANNA detector by rejecting thermal noise with deep learning, *JINST* **17** (03), P03007, [arXiv:2112.01031 \[astro-ph.IM\]](#).
 - [138] A. Coleman *et al.* (RNO-G), Enhancing the Sensitivity of RNO-G Using a Machine-learning Based Trigger, *PoS ICRC2023*, 1100 (2023).
 - [139] I. Esteban, M. C. González-García, M. Maltoni, T. Schwetz, and A. Zhou, The fate of hints: updated global analysis of three-flavor neutrino oscillations, *JHEP* **09**, 178, [arXiv:2007.14792 \[hep-ph\]](#).
 - [140] I. Esteban, M. C. González-García, M. Maltoni, T. Schwetz, and A. Zhou, <http://www.nu-fit.org/?q=node/256> (2022), NuFit 5.2.
 - [141] K. Fang, K. Kotera, K. Murase, and A. V. Olinto, Testing the Newborn Pulsar Origin of Ultrahigh Energy Cosmic Rays with EeV Neutrinos, *Phys. Rev. D* **90**, 103005 (2014), [Erratum: *Phys. Rev. D* **92**, 129901 (2015)], [arXiv:1311.2044 \[astro-ph.HE\]](#).
 - [142] P. Padovani, M. Petropoulou, P. Giommi, and E. Resconi, A simplified view of blazars: the neutrino background, *Mon. Not. Roy. Astron. Soc.* **452**, 1877 (2015), [arXiv:1506.09135 \[astro-ph.HE\]](#).
 - [143] K. Fang and K. Murase, Linking High-Energy Cosmic Particles by Black Hole Jets Embedded in Large-Scale Structures, *Nature Phys.* **14**, 396 (2018), [arXiv:1704.00015 \[astro-ph.HE\]](#).
 - [144] J. Heinze, A. Fedynitch, D. Boncioli, and W. Winter, A new view on Auger data and cosmogenic neutrinos in light of different nuclear disintegration and air-shower models, *Astrophys. J.* **873**, 88 (2019), [arXiv:1901.03338 \[astro-ph.HE\]](#).
 - [145] M. S. Muzio, M. Unger, and G. R. Farrar, Progress towards characterizing ultrahigh energy cosmic ray sources, *Phys. Rev. D* **100**, 103008 (2019), [arXiv:1906.06233 \[astro-ph.HE\]](#).
 - [146] X. Rodrigues, J. Heinze, A. Palladino, A. van Vliet, and W. Winter, Active Galactic Nuclei Jets as the Origin of Ultrahigh-Energy Cosmic Rays and Perspectives for the Detection of Astrophysical Source Neutrinos at EeV Energies, *Phys. Rev. Lett.* **126**, 191101 (2021), [arXiv:2003.08392 \[astro-ph.HE\]](#).
 - [147] M. S. Muzio, G. R. Farrar, and M. Unger, Probing the environments surrounding ultrahigh energy cosmic ray accelerators and their implications for astrophysical neutrinos, *Phys. Rev. D* **105**, 023022 (2022), [arXiv:2108.05512 \[astro-ph.HE\]](#).
 - [148] Q. Liu, D. F. G. Fiorillo, C. A. Argüelles, M. Bustamante, N. Song, and A. C. Vincent, Identifying Energy-Dependent Flavor Transitions in High-Energy Astrophysical Neutrino Measurements, (2023), [arXiv:2312.07649 \[astro-ph.HE\]](#).